Atmospheric drivers of Greenland surface melt revealed by Self Organizing Maps

J.R. Mioduszewski[1,2], A.K. Rennermalm[2], A. Hammann[2], M. Tedesco[3,4], E.U. Noble[3], J.C. Stroeve[5,6], T.L. Mote[7]

[1] Center for Climatic Research, University of Wisconsin - Madison, Madison, Wisconsin, USA

[2] Rutgers, The State University of New Jersey, New Brunswick, New Jersey, USA

[3] The City College of New York, City University of New York, New York, USA

[4] Lamont Doherty Earth Observatory of Columbia University, New York, USA

[5] National Snow and Ice Data Center, Boulder, Colorado, USA

[6] Centre for Polar Observation and Modelling Pearson Building, University College London, London, UK

[7] University of Georgia, Athens, Georgia, USA

Corresponding author: J. R. Mioduszewski, Center for Climatic Research, University of Wisconsin, Madison, WI 53706. (jmioduszewsk@wisc.edu)

Key Points:

Surface melt anomalies correspond with anomalies in energy advection and the local energy balance.

Atmospheric patterns that enhance surface melt have increased in frequency in the last 36 years.

Accelerating Greenland melt partially due to synoptic changes, but mostly to Arctic warming.

Abstract

Recent acceleration in surface melt on the Greenland ice sheet (GrIS) has occurred concurrently with a rapidly warming Arctic and has been connected to persistent, anomalous atmospheric circulation patterns over Greenland. To identify synoptic setups that favor enhanced GrIS surface melt and their decadal changes, we develop a summer Arctic synoptic climatology by employing self organizing maps (SOM). These are applied to daily summer 500 hPa geopotential height fields obtained from the Modern Era Retrospective Analysis for Research and Applications (MERRA) reanalysis product from 1979 to 2014. Particular circulation regimes are related to meteorological conditions and GrIS surface melt estimated with outputs from the Modèle Atmosphérique Régional (MAR).

Our results demonstrate that positive height anomalies near Greenland are associated with the largest positive surface melt anomalies, and are associated with wind, temperature and humidity patterns indicative of strong meridional transport of heat and moisture. We find an increased frequency in a 500 hPa ridge over Greenland coinciding with a 63% increase in GrIS melt between the 1979-1988 and 2005-2014 periods. For the entire ice sheet, 75.0% of melt changes between these time periods can be attributed to thermodynamics (Arctic warming), 17% to dynamics (circulation pattern frequency), and 8.0% to dynamics acting on thermodynamics. These results are confirmed by an analysis of melt changes over all 5-year periods between 1979 and 2014, which demonstrates that increased surface energy fluxes, temperature, and moisture separate from changes in synoptic pattern contributed more to melt even in the 2007-2012 period of most favorable dynamics.

1. Introduction

Recent studies have indicated that the Greenland ice sheet (GrIS) is experiencing negative mass balance, with an acceleration in mass loss due to increased surface melt resulting in runoff [*Box et al., 2006*; *Mote* 2007; *van den Broeke et al.*, 2009; *Fettweis et al.*, 2011; *Hanna et al.*, 2013a; *Hanna et al.*, 2013b; *Hanna et al.*, 2014]. Significant trends in ice sheet runoff are observed after 1990 [*Ettema et al.*, 2009] and have been attributed to global warming (Hanna et al. 2008). The areal coverage of melt has also expanded significantly up the ice sheet in the summer months and the melt season has lengthened since 1972 [*Box et al.*, 2006; *Mernild et al.*, 2011]. These changes have occurred simultaneously with those in the large-scale atmospheric circulation patterns and to the ice sheet surface energy balance. In this context, the relationship between increased surface melt and its atmospheric and energy balance drivers, including the influence of a warming Arctic, is still an area of active research.

The mechanisms that drive GrIS surface melt range from hemispheric-scale energy transport via synoptic systems to local-scale heat and moisture advection. To a first order approximation, variations in summer melt are linked to the strength and frequency of anticyclonic circulation and high pressure patterns over Greenland and the North Atlantic [*Mote*, 1998a; *Mote*, 1998b; *Fettweis et al.*, 2011; *Fettweis et al.*, 2013; *Hanna et al.*, 2013a]. The Greenland Blocking Index (GBI) is a metric for these circulation patterns over Greenland [*Fang*, 2004], and is found to be an optimal predictor of summer melt [*McLeod and Mote*, 2015]. In addition to the increased warm air advection, atmospheric blocking and anticyclonic flow produces subsidence, limited summer snowfall, and increased shortwave (SW) radiation, all enhancing summer mass loss [*Rajewicz and Marshall*, 2014].

Recent sea ice loss could possibly have an impact on the GrIS mass balance via

mechanisms ranging from local advection of warmer and moister air, increased precipitation, and synoptic-scale changes altering air mass advection and storm tracks [*Koenig et al.*, 2014; *Day et al.*, 2013]. Sea ice variability is strongly tied to patterns of turbulent heat flux and subsequent surface temperature anomalies [*Deser et al.*, 2000; *Rinke et al.*, 2006] and has been statistically linked to summer ice sheet melt [*Rennermalm et al.*, 2009; *McLeod and Mote*, 2015]. Aside from turbulent transfer from the ocean, North Atlantic sea surface temperatures (SST) offer a mechanism for influencing circulation patterns and melt conditions through impacts on the polar front and meridional flow patterns [*Hall et al.*, 2015]. The Atlantic Multidecadal Oscillation (AMO) is a metric for these SST anomalies, switching to its positive mode around 1995. The positive AMO correlates significantly with positive summer temperature anomalies in Greenland [*Hanna et al.*, 2013a; *Rajewicz and Marshall*, 2014] and has been implicated in GrIS summer melt via multiple linear regression [*McLeod and Mote*, 2015].

While the entire Arctic has warmed in recent decades [*Serreze and Francis*, 2006; *Serreze et al.*, 2009; *Pithan and Mauritsen*, 2014; *Overland et al.*, 2015a], the atmospheric circulation has also become more persistently conducive to Greenland melt in the last decade. The resultant increased poleward heat advection appears to have served as the dominant driver of some of Greenland's record surface melt in the most recent years, particularly 2007-2012 [*Fettweis et al.*, 2011a; *Hanna et al.*, 2013b; *Hanna et al.*, 2014; *Neff et al.*, 2014]. The summer of 2007 began a series of summers with record mass loss amounting to an increase in runoff of 30% in the western ablation zone [*van Angelen et al.*, 2014], though *Mote* [2007] found that coastal station temperatures were no warmer than those of several summers in the previous five when surface melt was not nearly as extensive. In 2012, a series of exceptional blocks developed over Greenland through mid-July causing the record melt [*Neff et al.*, 2014], and simultaneously

one of the lowest NAO index values since 1900 [*Hanna et al.*, 2015; *Tedesco et al.*, 2013]. The warming of 2007-2012 over the GrIS didn't occur everywhere in the Arctic because it was mainly driven by anomalies in dynamics and persistent anticyclonic flow over Greenland impacting local heat transport [*Overland et al.*, 2012; *Fettweis et al.*, 2013; *van Angelen et al.*, 2014]. Anticyclonic flow over Greenland strongly favors positive temperature anomalies over western Greenland but weak anomalies on the east side of the ice sheet and cooler temperatures as near as Svalbard [*Fettweis et al.*, 2013].

As the Arctic warms and circulation patterns shift, both in response to anthropogenic warming and due to natural variability, it is still unclear exactly how much of the recent acceleration in GrIS surface melt can be attributed to each of these processes. Various methods in synoptic climatology have been applied to this problem, including cluster analysis [*Mote*, 1998b] and a circulation type classification [*Fettweis et al.*, 2011]. *Fettweis et al.* [2013] found that changes in circulation have accounted for about two thirds of the warming near Greenland since 1983, and the frequency of anticyclonic circulation over the GrIS increased significantly in the last two decades. Similarly, up to half the inter-annual variability in summer air temperature and associated melt was found to be explained by the strength and frequency of anticyclonic systems, while "background" warming explained up to a quarter of this variability [*Rajewicz and Marshall,* 2014].

This study investigates in detail the controls on summer Greenland ice sheet surface melt in the 1979 to 2014 period by developing a synoptic climatology using self organizing maps (SOM) of 500 hPa geopotential heights derived from Modern Era Retrospective Analysis for Research and Applications (MERRA). Regional climate model outputs from Modèle Atmosphérique Régional (MAR) around Greenland are analyzed with respect to SOM results

over the 1979 – 2014 period to describe the Arctic atmospheric circulation and energy balance and quantify its relationship with GrIS surface mass loss. Specifically, we examine the relative roles of energy balance terms from individual synoptic patterns that drive summer melt via their breakdown across SOM nodes. We also parse the changes in surface mass loss through time into a thermodynamic component, representing changes in atmospheric state, and a dynamic component, representing changes in specific weather pattern frequencies. From this, we are able to assess the evolution of the relative contribution of each to total mass loss throughout our 36-year study period, as well as which components of the energy balance are driving these changes. Given the significance of the thermodynamic component, we also identify the primary forcings responsible for its contribution to increased surface melt.

2. Data

Sea level atmospheric pressure (SLP) and 500 hPa geopotential height fields were obtained from MERRA reanalysis to diagnose atmospheric circulation patterns and their relationship with surface meteorological and hydrologic variables. MERRA is NASA's state-of-the-art reanalysis product generated with the Goddard Earth Observing System Model, version 5 (GEOS-5) data assimilation system [*Bosilovich et al.*, 2011; *Cullather and Bosilovich 2011, 2012*; *Rienecker et al.*, 2011]. It is forced by the atmospheric model, with inputs assimilated from a wide range of remote sensing observations in addition to meteorological surface observations, and run on a 1/2° latitude by 2/3° longitude global grid with output at 6 hour intervals. Data were aggregated to daily for this study for the time period 1979 to 2014 for JJA. MERRA has been evaluated extensively since its release [*Cullather and Bosilovich*, 2012; *Kennedy et al.*, 2011; *Reichle et al.*, 2011] and has compared favorably with other reanalysis products in the Arctic

[e.g. *Zib et al.*, 2012; *Cullather and Bosilovich*, 2011; *Lindsay et al.*, 2014].

GrIS meltwater production, energy balance and near-surface (approximately 10 m) and 700 hPa meteorological fields between 1979 and 2014 were estimated by MAR v3.2 regional climate model data for Greenland [*Tedesco et al.*, 2014]. MAR is a three-dimensional coupled atmosphere-land surface model using NCEP/NCAR global reanalysis at its lateral boundaries to predict the evolution of the land-atmosphere system at 6-hour intervals. MAR's atmospheric model is coupled to the 1-D Surface Vegetation Atmosphere Transfer scheme, SISVAT [*Gallée and Schayes*, 1994; *De Ridder and Gallée*, 1998], which simulates surface properties and the exchange of mass and energy between the surface and the atmosphere in both directions. A sea ice mask (0-100%) and a sea surface temperature mask, updated every 6 hours and obtained from reanalysis data, incorporates sea ice data derived from spaceborne microwave observations. MAR 3.2 has been validated through comparison with ground measurements [e.g. *Lefebre et al.*, 2003; *Gallée et al.*, 2005; *Lefebre et al.*, 2005] and satellite data [e.g. *Fettweis et al.*, 2005, 2011a; *Tedesco et al.*, 2011], and applied to simulate long-term changes in the GrIS SMB and surface melt extent (*Fettweis et al.*, 2005, 2011a; *Tedesco et al.*, 2008, 2011]. Model simulations are run on a polar stereographic projection with an approximate grid cell size of 36 x 36 km.

MAR data at two atmospheric levels are used because they provide different insights. First, 700 hPa are used because this height is above the boundary layer over all of the ice sheet except interior parts of the accumulation zone, and is well suited for estimating synoptic- and hemispheric-scale advection. This level is also high enough to provide insight into the steering patterns of synoptic systems, which are normally assessed between 700 hPa and 500 hPa. Second, data at approximately 10 m (sigma = 0.9996) are used to infer temperature and moisture advection at the surface and potentially any local-scale advection from offshore to the ice sheet.

Meltwater production data were only used for grid cells classified by MAR as having more than 99% ice sheet, which effectively masks the tundra region (714, 096 km^2) of Greenland from our study. MAR simulates meltwater production as a floating point variable, which are rounded to integers to save computer storage space for the model output. This rounding makes it impossible to distinguish if small values for meltwater production are representing actual melt. Thus, in line with previous MAR adoptions [*Fettweis et al.,* 2011a, Figure 2], meltwater production values less than 1 mm day^{-1} are recoded to zero. When meltwater production is averaged over the ice sheet, results are given in gigatons (Gt) to allow for ease of comparison with previous literature. The resulting daily meltwater production is summed over all nodes and all 92 days of JJA, then multiplied by 1,296 km^2 (the area of a grid cell) and divided by the density of water (999.8 kg m^{-3}) to convert to Gt summer^{-1}. However, we emphasize that this is a rough and likely conservative estimate of mass loss from surface melt, and is intended only to be compared within our own results than as a new estimate of total mass loss between two time periods. This is due to dataset limitations, exclusion of months outside of JJA, and the masking procedures discussed above.

3. Self Organizing Maps Methodology

SOM analysis is employed to analyze atmospheric circulation patterns and the atmospheric and surface variables that correspond to the different identified circulation regimes. SOMs are neural network algorithms that use unsupervised classification to perform non-linear mapping of high-dimensional datasets [*Kohonen*, 2001]. Similar to cluster analysis, this method

effectively reduces a large dataset into fewer representative samples without assumptions about the final structure of these samples. This method has been used previously in similar studies of Arctic synoptic climatology and its changes [*Cassano et al.*, 2006; *Skific et al.*, 2009; *Higgins and Cassano*, 2009; *Johnson et al.*, 2008; *Mills and Walsh*, 2014; *Horton et al.*, 2015] as well as specifically over the Greenland domain [*Schuenemann et al.*, 2009; *Schuenemann and Cassano*, 2009].

Here, SOM analysis is done on the field of 500 hPa geopotential height anomalies derived from MERRA across the northern hemisphere north of 60°N to develop a summer synoptic climatology of the Arctic. This method uses training data drawn from daily JJA 500 hPa height anomalies, yielding a "master" SOM map with 30 nodes that represents the spectrum of synoptic patterns. The number of nodes is typically user-defined and is a trade-off between forcing the daily circulation pattern into a category that is a poor fit (too few nodes) and displaying an overwhelming amount of data (too many nodes). For this application, 30 nodes was empirically determined to offer a sufficient balance between these potential issues. Anomalies of 500 hPa geopotential heights were calculated relative to the individual grid cell for each day of the summer, and the data were weighted by the square root of the cosine of the latitude to account for the poleward grid cell area bias in the model grid.

Numerically, the best matching node for each input date is determined by computing the Euclidean distance of each example vector and matching it to the node with the most similar weight vector within the neural network (i.e., the ultimate master map). Thus, every date in the record is assigned a best matching node, so any field from the same date can be composited over each node on the master map and displayed visually. In this way, MAR output fields of meltwater production, SW and longwave (LW) radiation, temperature, specific humidity,

turbulent fluxes, cloud fraction, and wind were mapped onto the resulting master map.

Because significant trends exist in some of the 500 hPa height patterns, change in node frequency and its significance over two periods of interest was calculated for these nodes. This change was calculated by subtracting the averaged frequency over 1979-1988 from that of 2005-2014. Statistical significance was calculated by generating a binomial distribution following *Cassano et al.* [2007], testing the hypothesis that the difference of the node frequencies between the two time periods is zero. If the test statistic exceeds 1.96, we can reject the null hypothesis at the 95% confidence level and consider the change in node frequency between time periods to be significant. The test statistic to test for changes in this frequency assumes two random, independent, binomial processes and is given by:

$$\frac{(p_1 - p_2)}{\sqrt{\frac{p_1(1-p_1)}{n_1} + \frac{p_2(1-p_2)}{n_2}}}$$

where $p_1(1-p_1)/n_1$ and $p_2(1-p_2)/n_2$ are estimators of the node frequency variances, p_1 and p_2 are the frequency of occurrence in each time period, and n_1 and n_2 are the number of days in each time period ($n_1 = n_2 = 920$). This test overestimates degrees of freedom because it does not account for autocorrelation in the time series of 500 hPa geopotential heights, so the effective degrees of freedom are approximated by dividing n_1 and n_2 by 5. This indicates that the atmosphere tends to remain in a similar circulation regime for about 5 days, which was estimated empirically from the autocorrelation of this time series over the summers of interest. This results in fewer degrees of freedom and therefore a test statistic of greater magnitude, raising the threshold to achieve statistical significance.

To understand what processes have driven the observed increase in mass loss, the total

temporal change in GrIS mass loss was parsed into three components: 1) dynamic change, 2) thermodynamic change, and 3) a combination of both. These components were identified by calculating 1) contribution from the change in daily frequency of a given SOM node, 2) the contribution due to the change in the node-averaged value of melt, and 3) the contribution from a combination of these two terms, following a methodology developed by *Cassano et al.* [2007] and employed by others [e.g. *Higgins and Cassano*, 2009; *Skific et al.*, 2009; *Horton et al.*, 2015]. The equation is as follows:

$$\Delta M = \sum_{n=1}^{N} (\Delta f_n M_{init,n} + f_{init,n} \Delta M_n + \Delta f_n \Delta M_n) \tag{1}$$

Where ΔM is the total change in ice sheet-averaged meltwater (Gt), Δf is the change in node frequency between two periods, f_{init} is the node frequency of occurrence in the initial period, M_{init} is the node-averaged meltwater in the initial period, ΔM is the change in meltwater between two periods, and n are the nodes.

The first term, $\Delta f_n M_{init,n}$, referred to as the dynamic change component, is the contribution to ΔM that results from changes in SOM pattern frequency. This term reflects a change in the distribution of the SOM nodes, i.e. a change in the 500 hPa fields residing in them. The second term, $F_{init,n}\Delta M_n$, referred to as the thermodynamic term, relates to temporal changes between two periods of interest in melt averaged over all days belonging to a node. This term is numerically equivalent to the difference between the averaged melt anomaly fields for a given SOM pattern. The final term in Eq. 1 is the combination term, and it includes the contribution arising from

changes in node frequency acting on changes in node averaged melt, which tends to be the smallest term.

4. Results

4.1 SOM Analysis of 500 hPa Geopotential Heights

SOM analysis was performed on daily anomalies of the 500 hPa geopotential height field in JJA from MERRA reanalysis to better understand which atmospheric patterns are most conducive to high and low GrIS meltwater production (Fig. 1). The master SOM organizes these fields into a range of patterns that occur during the summer months in the Arctic, with the strongest anomalies generally on the periphery, and particularly in the upper left and lower right corners. The synoptic patterns are split primarily between high and low height anomalies over Greenland west across Baffin Bay to the Beaufort Sea. SLP was next mapped to each node, meaning that the spatial dataset of these anomalies was composited and displayed visually at the same node position for each date where the daily SLP data most closely match a given node. This shows the surface expression of these mid-level height anomalies, which reflect the 500 hPa patterns very closely (Fig. 2). Therefore, high surface pressure patterns over Greenland roughly correspond to to a mid-level ridge and warmer surface conditions, and a trough and colder surface conditions with low surface pressure overhead.

Because MAR variables are used for most of the remainder of the analysis, it is necessary to evaluate the consistency between MAR and MERRA synoptic characterizations. To do this, MAR 500 hPa geopotential height anomalies were mapped onto the MERRA-derived master SOM over its reduced domain (Fig. 3a). The results show that MAR-derived anomalies in each

node are qualitatively very similar, in some nodes nearly identical, to those in Fig. 1 using MERRA training data. The node-averaged root mean square error (RMSE) using differences between MAR and regridded MERRA height anomalies reflect minor differences, with maximum RMSE values under 8 m centered over Greenland (Fig. 3b). Away from Greenland, the RMSE is under 4 m, indicating that differences between the two datasets are likely, in this domain, primarily due to model differences in the handling of the ice sheet. This affords us a high level of confidence in our ability to draw conclusions from MAR variables based on the nodes generated with Arctic-scale MERRA data.

Meltwater production anomalies were next mapped onto each node (Fig. 4). It is evident that there are preferred nodes for both positive and negative melt anomalies corresponding to positive and negative heights, respectively, over the Greenland area. This node preference for melt anomalies was further demonstrated by analyzing the node distribution of extreme area-averaged meltwater production (Fig. 5). Only dates exhibiting meltwater production of more than 1 standard deviation above or below the mean (calculated relative to each of the 92 days) were tabulated and displayed on the charts. This identifies the synoptic patterns that favor large melt events (Fig. 5a) or lack of melt (Fig. 5b) over the ice sheet. Positive melt anomalies mostly occur with a ridge in the vicinity of Greenland and extending north and west toward the Beaufort Sea. Negative melt anomalies occur in nearly the opposite pattern; a trough over Greenland and Baffin Bay. These height patterns are associated with anomalies in other meteorological fields such as temperature, humidity, and wind direction, which serve as the dominant physical control on GrIS melt, and these can be mapped to each node in the same way as in Figs. 2 and 4. For ease of display, we integrate the meteorological fields for the three nodes with the highest melting, (1,1),

(2,3) and (5,1), and the three nodes with the lowest melting (1,6), (3,4), and (4,5). This is presented below.

4.2 Energy Balance Analysis

Anomalies of energy balance variables were next calculated relative to the 36-year mean of each grid cell and day of the summer. SW radiation over much of the ice sheet exhibits weak positive anomalies in high melt nodes (Fig. 6a). In contrast, solar radiation has a tendency toward negative anomalies in low melt nodes; particularly across central and eastern Greenland (Fig. 6b,c). Positive anomalies of downwelling LW radiation are found over much of Greenland and surrounding seas (Fig. 6d), with the opposite pattern of the same magnitude occurring in low melt nodes (Fig. 6e,f). Eastern Greenland, however, exhibits weak positive anomalies in LW radiation in low melt nodes, particularly relative to high melt nodes. Mapping cloud fraction to these nodes shows that clouds are at least partially responsible for these radiation anomalies (Fig. 6g-i). Clearer conditions prevail over the ice sheet in high melt nodes corresponding to positive SLP anomalies (Fig. 2) and matching to a lesser extent with the radiation anomalies. Positive anomalies in cloud fraction exist well off the west and southwest coasts, coinciding with positive LW anomalies. Negative melt nodes exhibit positive cloud anomalies over all of the ice sheet except north-central regions and the southern tip, and negative anomalies off the west and southwest coasts, again agreeing with above analysis.

Sensible and latent heat fluxes mapped to the SOM nodes show negative (downward) anomalies in high melt nodes both over the ice sheet and over the same maritime regions where cloud and radiation anomalies were centered, with anomalies of the opposite sign over the

14 of 46

Greenland Sea (Fig. 6j). Low melt nodes express the opposite pattern and of similar magnitude (Fig. 6k,l). This is in agreement with the melt anomalies, given that there is more energy via sensible heat entering the ice in high melt nodes and vice versa in low melt nodes. Sensible heat flux anomalies are particularly pronounced in a narrow region by the ice sheet edge stretching along the entire west coast. Latent heat fluxes are similar to sensible fluxes over maritime regions representing evaporation anomalies, but are very weak in comparison on the GrIS (Fig. 6 m-o). Given that daily averages are used, it is likely that this is partially due to latent heat anomalies getting averaged out in the diurnal melt-freeze cycle of the ablation zone.

4.3 Surface and 700 hPa Meteorology

In the next analysis, winds at two atmospheric levels (700 hPa and approximately 10 m) were plotted for each set of the extreme nodes and averaged for the high, (1,1), (2,3), and (5,1) and low, (1,6), (3,4), and (4,5) melt nodes similar to the meteorological variables presented above. These wind vector maps were overlaid on composite maps of temperature and specific humidity at these respective levels. Together, these allow for inference of temperature and moisture advection.

The atmospheric circulation pattern at 700 hPa in each set of nodes is nearly opposite to one another (Fig. 7a,b). In high melt nodes, an upper level ridge and surface high pressure translates to southerly winds on the west side of Greenland, circulating over or north of Greenland with a northerly or northwesterly flow on the northeast side of Greenland (Fig. 7a). This facilitates advection of air from the south and southwest, particularly across southwestern Greenland. Additionally, this type of wind circulation tends to be aligned with the persistent, more

mesoscale anticyclonic circulation existing over the interior ice sheet at the surface (and extending into the atmosphere beyond 700 hPa) which is responsible for the very persistent downsloping wind along the ice sheet edge.

In low melt nodes, stronger winds south of Greenland across the North Atlantic persist, showing how the Westerlies are strengthened (or more persistent) in this pattern when SLP is lower over the ice sheet (Fig. 7b,c). Winds in this pattern tend to curve around southern rather than northern Greenland, bringing a northwesterly flow to western Greenland and a southwesterly flow to eastern Greenland. The anticyclonic flow over the ice sheet still exists, but acts against the large-scale atmospheric circulation of low melt nodes. This facilitates cyclonic rotation off the southeast coast (the Icelandic Low) and a barrier wind setup, whereas this low pressure system is not visible during high melt nodes in Fig. 7a.

The 700 hPa temperatures are several degrees warmer over most of Greenland, particularly the western half, in high melt nodes compared to low melt nodes (Fig. 7a-c). Any difference in temperature at this level can be attributed to large-scale advection since turbulent fluxes from the surface are generally confined to the boundary layer, which does not extend to the 700 hPa atmospheric level. The more zonal flow in low melt nodes indicates that heat is transported largely from west to east (south of Greenland) without influencing Greenland and keeping it relatively cool (Fig. 7b,c). In contrast, flow in high melt nodes and the warmer temperatures in southern and eastern Greenland indicate that heat is advected northward from the warmer oceans just to the south (Fig. 7a). In eastern and northern Greenland, the temperature difference between high and low nodes is not as great, which is most likely related to a weaker preference in wind direction.

Specific humidity at 700 hPa exhibits a similar pattern as temperature, with much moister air southwest of Greenland suggesting northward moisture advection (Fig. 7d-f). However, most of this influence appears to be limited to southern and western Greenland, but extends well up the ice sheet on the stronger southerly winds (the anticyclone over the ice sheet is enhanced by large-scale winds in the same direction).

Near the surface at approximately 10 m, the anticyclone over the GrIS dominates and the wind blows from the ice sheet interior along much of the ice edge in both high (Fig. 7g) and low melt nodes (Fig. 7h). In other words, the synoptic setup associated with high and low melt nodes does not appear to interfere with these strong, near-surface, downsloping winds. Otherwise, winds are a lot more variable in direction on the Greenland coast likely primarily due to frictional effects and complex boundary layer processes, e.g. in southwestern Greenland [*Orr et al.*, 2005]. The wind is more variable in Baffin Bay and farther north in the Greenland Sea. Ocean winds are still of opposite direction in high and low melt nodes in the North Atlantic with strong Westerlies in Fig. 7h. The Icelandic Low surface expression is also found near the southeast coast, with an easterly wind curving around the southern tip, similar to 700 hPa patterns (Fig. 7b).

Similar to the large differences in 700 hPa temperature and specific humidity between high and low melt nodes, these differences are found at the near-surface level but centered over Greenland due to the moderating influence of the ocean and sea ice (Fig. 7g-l). Temperatures are 3-5 °C warmer over most of Greenland, particularly the western half, at 10 m in the high melt nodes (Fig. 7g-i). Specific humidity differences over the ice sheet are relatively minor between high and low melt nodes (Fig. 7j-l), with a maximum of approximately 0.5 g kg^{-1} over the west side of the GrIS.

4.4 SOM Node Frequency and Trends   The node frequency chart (Fig. 8a) displays

the percentage of total days that match most closely to each node relative to total days in the pe-

riod (n = 3312). A higher frequency of data is represented in periphery nodes with fewer occur-

ring in the center. Given that the expected frequency for a SOM chart of this size (N = 30) is

(1/N) x 100 = 3.33%, most periphery nodes are above this value and most inner nodes are below.

To assess the change of SOM pattern frequency over time, the first and last ten years of

the period (1979-1988 and 2005-2014) were chosen. The change in frequency was obtained by

subtracting the subset of dates that best match a given node only in these two periods, giving the

resulting change in node frequency (Fig. 10b). Several nodes exhibit statistically significant

changes at a 95% confidence level (indicated in red), particularly nodes (3,1), (4,1), and (5,1)

which correspond to strong positive height anomalies over the Greenland side of the Arctic. Oth-

erwise, nodes (1,5) and (5,6) show significant decreases in frequency, and several others de-

crease at a similar magnitude but without statistical significance. Most of the nodes that have de-

creased in frequency are characterized by positive height anomalies over northern Europe as well

as Siberia and opposing negative anomalies on the opposite side of the hemisphere, which are

patterns that tend to suppress melt events over the GrIS.

4.5 Partitioning Mass Loss Change into its Components

The node-averaged change in meltwater production, and therefore ice sheet surface mass

loss, between these two periods shows that the strongest increases occurr in the nodes in the first

column, while a few nodes exhibit decreases (Fig. 9a). Summed over all nodes, there is an additional 103.2 Gt summer^{-1} of mass loss, which is an average increase of 62.8% from 1979-1988 to 2005-2014 (from Fig. 10a). Following equation (1), the total change in mass loss in each node was split up into three components: 1) increases within the circulation regime (thermodynamic term, Fig. 9b); 2) change in the frequency of this regime (dynamic term, Fig 9c); and 3) a combination of both (Fig. 9d).

The meltwater production change from thermodynamics is positive in almost all nodes, and sums to 77.5 Gt more ice loss (75.0% of the total; Fig. 9b). This indicates that the amount of melt that occurs in a fixed synoptic pattern has increased between time periods, primarily due to more favorable conditions for melting (e.g. increased solar radiation, LW radiation, sensible heat fluxes, and lowered albedo). Given an otherwise equal change in these conditions, this term will be larger in nodes with a higher initial frequency of occurrence.

The dynamic contribution to meltwater change is an increase of 17.4 Gt ice loss (16.9%) between these time periods (Fig. 9c). However, in each individual node, the magnitude of change tends to be higher than that from thermodynamics, but of varying sign, so some of the changes cancel out. This is because some of the nodes have become more frequent and some less frequent, as would be expected. Negative changes from dynamics occur when the circulation pattern has shifted toward one less conducive to GrIS melt, while positive changes occur due to the opposite type of pattern change. The nodes in the left column contribute a large proportion of the total increase due to dynamics, (43.8 Gt), and this accounts for a large percentage of the total increase from these nodes. Furthermore, the three nodes identified as increasing significantly (i.e. (3,1) (4,1), and (5,1) from Fig. 8b) contribute the majority to this term (38.6 Gt meltwater).

Finally, the combination term (Fig. 9d) is about an order of magnitude smaller in most nodes which is typical of this term (e.g. Cassano et al. 2007). The node-summed mass loss is 8.3 Gt meltwater (8.0%), with a lot of changes that cancel out as in the dynamic term.

Part of the increase in mass loss over the time period 1979-1988 to 2005-2014 is due to increased melt extent. The change in melt extent can indirectly be determined from the number of MAR grid cells used to calculate total meltwater production, because only MAR grid cells in which meltwater production exceed 1 mm day^{-1} are included. Out of a total of 1137 possible ice sheet grid cells, the 92-day mean change in daily grid cells exceeding this 1 mm day^{-1} threshold increased from 273 in the 1979-1988 period to 323 in the 2005-2014 period (18.3% increase).

The breakdown of meltwater production changes into total change and its three components was next assessed using pairs of all possible 5-year time periods in the 1979-2014 study period to identify more nuanced temporal patterns (Fig. 10b-e). In this assessment, the node-summed total mass loss change and its three components are calculated for each pair of 5-year periods. Each point on the chart represents the difference between a pair, where the first 5-year period is on the y-axis and the latter is on the x-axis (Fig. 10b-e). The chart is oriented such that the amount of time between time periods increases perpendicular to the dashed lines toward the lower right. Therefore, if mass loss were increasing at the same rate through time, the shading would transition from blue at the initial-year line in the middle to orange and yellow in the lower right corner where more than 25 years separates the time periods. This pattern is not observed, however, and it is apparent that meltwater production has accelerated in the most recent decade with more than 120 Gt summer^{-1} more ice lost in recent 5-year periods than those as recently as the late 1990's. Otherwise, there are only small increases or even decreases in meltwater produc-

tion using a final time period up to the mid-1990's. Decreasing melt occurs early in the study period, indicating that there was slightly more melt in the mid-late 1980's than just afterwards. Using an initial time period between 1985 and 1990, Fig. 10b shows lower mass loss values relative to adjacent periods, indicating that there was more melt in this period than prior to or just after it, hence the lower (even negative) differences relative to later time periods.

The thermodynamic component of this change in meltwater production (Fig. 10c) is expressed in a similar pattern as the total change, but the magnitude is somewhat smaller than that of the total change. This suggests that the thermodynamic component comprises the majority of the total change in mass loss, but that the other two components play a minor additional role in driving changes to melt.

The melt change from dynamics (Fig. 10d) tends to be smaller than the thermodynamic component, which is again due to positive and negative change in frequencies canceling as demonstrated in Fig. 9c. The most notable result here is that the period centered from about 2008-2012 has been much more favorable for Greenland mass loss than prior periods. While the favorable dynamics of this period has been well established [*Overland et al.*, 2012; *Rajewicz and Marshall*, 2014; *Belleflamme et al.*, 2015], this analysis quantitatively places this time period in the context of the last 36 years specifically relative to GrIS surface melt. The dark yellow shading does not extend to the right edge of Fig. 10d, evidence of the 2013-2014 summers with less persistent ridging near Greenland to generate strong melt events [*Jeffries and Richter-Menge*, 2015].

Finally, the combination term is very similar to Fig. 10c in terms of its pattern and also magnitude (Fig. 10e). It is typically negative because it is the product of the thermodynamic change, mostly positive, and the dynamic change, which is negative in approximately half the

nodes. The resulting node-summed values consequently cancel out to some degree as with the dynamic component, but the individual node magnitudes of the combination term are not as large (e.g. Fig. 9d).

4.6 Attribution of the Thermodynamic Change

Given that 75% of surface melt change between these two time periods can be attributed to thermodynamics, we examine this particular component to clearly identify the forcings that have most contributed to its increased role in mass loss. This is done by calculating the node-averaged differences in a variety of energy balance and meteorological variables, composited over the three nodes in Fig. 9b with the greatest increase in mass loss due to thermodynamics: nodes (1,1), (1,3), and (1,5).

There are nearly domain-wide increases in downwelling LW radiation, adding an average of 10-20 W m^{-2} to the surface of the GrIS (Fig. 11b). This has occurred largely while cloud fraction has decreased (Fig. 11d) over all but the northwestern part of the ice sheet, resulting in an increase in insolation in the same regions (Fig. 11a) comparable in magnitude to that in LW radiation. Net radiation shows a spatial pattern of change of the greatest increases over the tundra and ablation zones, and very weak changes over the remainder of the ice sheet with no substantial decreases anywhere (Fig. 11c).

As a result of these changes in radiative forcing, the near-surface temperature and humidity have increased substantially over the entire domain in these nodes, an average of more than 3 °C (Fig. 11g) and nearly 0.5 g kg^{-1} (Fig. 11h), respectively, over land for a fixed synoptic pattern. Temperature increases are reflected in the change in sensible heat fluxes (Fig. 11e), which are

now more negative in the ablation zone of western Greenland in particular, and positive over the tundra. This indicates there is more energy moving into the ice sheet to drive surface melt, while warming surface temperatures over the tundra are generating greater instability and more upward transfer into the atmosphere. Changes in latent fluxes are comparatively weak (Fig. 11f), and would likely be only responding to melt-related hydrologic changes that are responding to thermodynamic changes.

5. Discussion

Our study shows that while the atmospheric circulation patterns that result in high melting have increased in frequency (i.e. dynamic change), total GrIS surface mass loss is dominated by greater positive melt anomalies regardless of circulation regime (i.e. thermodynamic change). This reconciles previous studies showing major circulation changes as well as those demonstrating significant changes in the surface energy balance components. Specifically, we find that these thermodynamic changes are driven by radiation terms which have substantially increased near-surface temperature and humidity. Furthermore, we show that the circulation patterns most closely associated with positive melt anomalies correspond to anomalies of short- and longwave radiation modulated primarily by cloud cover distribution, as well as sensible heat fluxes that are most important in the southwestern ablation zone. Finally, while local-scale advection of heat and moisture from the ocean to the GrIS appears to be limited by strong katabatic winds, synoptic-scale energy advection above the boundary layer likely plays a large role in transporting the energy required to generate surface melt.

Turbulent fluxes are a dominant component of energy input in the lower ablation zone [*van den Broeke et al.*, 2011; *Franco et al.*, 2014], but using daily mean values can considerably suppress turbulent fluxes that are often both positive and negative throughout the diurnal cycle. Sensible fluxes directed into the ice appear appear to be a significant factor in high melt nodes, but their relative contribution is difficult to assess with this methodology. Regardless, this is supported by studies using in situ data showing that sensible heat flux can be the dominant control on surface melting in the ablation zone in Southwest Greenland [*van den Broeke et al.*, 2011]

Even when large-scale flow favors onshore winds and advection onto the ice sheet, the persistent downsloping flow off the ice may not allow for a marine influence, particularly in the upper ablation zone [*Noël et al.*, 2014]. Most of the lower ablation zone experiences these katabatic winds a majority of the time in the summer with directional constancy of the surface wind exceeding 80% [*Ettema et al.*, 2010; *van Angelen et al.*, 2011; *Gorter et al*., 2014], but there is still mixing of warmer air from the tundra. A barrier wind can be established under the right conditions primarily from the pooling of stable cold air past the ice edge contrasted with the relatively warm and unstable tundra air [*van den Broeke et al.*, 1994]. Barrier winds result in strong melting in the ablation zone by generating turbulence that is strong enough to overcome the thermal stratification of the surface layer, mixing warmer air down to the ice surface [*van den Broeke et al.*, 1996]. Synoptically, high pressure over Greenland is ideal for katabatic flow on the west side of the ice sheet, and the approach of a cyclone in Baffin Bay enhances southerly flow, allowing a barrier wind to form and enhance surface melt via turbulent mixing. However, in patterns with a northerly or northwesterly flow aloft, katabatic will be weaker and barrier winds typically disappear [*van den Broeke et al.*, 1996]. Although MAR, run at 36 km resolution, is unable

to resolve some of the boundary layer physics that allow for increased mixing of unstable and warm/moist tundra (and offshore) air, this is another mechanism by which these synoptic patterns both enhance and suppress surface melt in the ablation zone.

There are some significant changes in frequency of occurrence of SOM nodes between 1979-1988 and 2005-2014. Results suggest that changes in atmospheric circulation have resulted in an increasing frequency in ridging in this part of the Arctic, which has consequences in energy transport and surface conditions in these regions, as discussed above. Specifically, the three patterns that have become significantly more frequent are those with the strongest positive anomalies from Greenland to the pole, while those that have become significantly less frequent exhibit the opposite pattern. In support of this, the frequency of anticyclonic flow over the GrIS associated with a negative NAO was found to have doubled since the late 1990's by *Fettweis et al.* [2013], and the frequency of blocking in the North Atlantic may increase in the future as a result of a reduction in the meridional thickness gradient [*Francis and Vavrus*, 2015; Overland et al. 2015b]. All of this favors the continued increase in summer surface melt on the GrIS.

Between the first and last ten years of the study period, JJA surface mass loss has increased 63% with relative contributions of 75% from thermodynamics, 17% from dynamics, 8% from a combination. Much of the increase from dynamics is due to a few nodes in the left column of Fig. 1 increasing at statistically significant levels. The dynamic contribution of the individual nodes between the ten year periods is larger than the thermodynamic contribution. However, after taking the sum of the nodes, the thermodynamic component accounts for the majority of the changes because the change in nearly every node is positive. Even though the frequency of some of the nodes has decreased at a statistically significant level, the total change in mass loss

in these nodes is positive, arguing for the strength of the forcing generating the thermodynamic change.

The literature has identified some major circulation changes through our study period, and some of these are observed in our results based on Fig. 10d. There appear to be multiyear oscillation signals within the surface melt trends [*Abdalati and Steffen*, 2001], and *Bhattacharya et al.* [2009] find a change in melt patterns and variability in 1995, corresponding to a general trend upward in the NAO index. From 2007 to 2012 the Dipole Anomaly and the NAO have been in their negative modes which strongly support melt events on the GrIS [*Overland et al.*, 2012]. Aside from the 2007-2012 time period, there has been no persistence in the positive or negative mode of the NAO since 1979. *Rajewicz and Marshall* [2014] also found some differences in GrIS melt extent after 2001 responding to circulation changes, but this is not evident in Fig. 10. Finally, the AMO transitioned into its positive mode in the late 1990's and has been linked to GrIS melt anomalies [*Rajewicz and Marshall*, 2014; *McLeod and Mote*, 2015]. This is in agreement with Fig. 10, where the largest change in mass balance occurs when using an initial period just prior to that shift.

Changes in mass loss are driven mainly by processes occurring for a fixed circulation regime, implying that the same synoptic pattern has generated greater levels of melt. The breakdown is dominated by thermodynamics because this change in almost all the nodes is positive regardless of the change in frequency (e.g. Fig. 10c). Using the same methodology, *Skific et al.* [2009] and *Higgins and Cassano* [2008] also found the thermodynamic component to account for the majority (>95%) of the change between their time periods, but the larger Arctic domain was used, and rather than surface melt, analysis focused on precipitation, 1000 hPa heights,

cloud fraction, and LW radiation. The increased favorability of the mid-level atmospheric circulation for GrIS melt recently noted by *Fettweis et al.* [2013] and *Rajewicz and Marshall* [2014] qualitatively matches our results, though both studies attribute approximately twice as much of summer temperature variability (rather than specifically surface melt) over Greenland to these circulation changes than to thermodynamics via two relatively similar methodologies. The differences in attribution among studies are likely due to a combination of differences primarily in methods, time periods, and variables analyzed, though we have shown that the time period chosen (since 1979) makes little difference, as the thermodynamic component accounts for the majority of the mass loss (Fig. 10). Nonetheless, it is apparent that both processes have significant contributions to GrIS surface mass loss and should both be given careful consideration in projections of future ice sheet mass balance.

Results from Fig. 11 indicate that the primary thermodynamic drivers of increased surface melt are an increase in LW radiation despite a decrease in cloud fraction (and corresponding increase in insolation), increased net radiation, and substantially increased near-surface temperature and humidity at least in partial response to the increased incoming radiation. Interestingly, from Figs. 1 and 2, the synoptic patterns in these three nodes are not particularly similar, with SLP and height anomalies of opposing signs over Greenland in nodes (1,1) and (1,5). This allows interpretation of the results as a cross section of different patterns independent of any change in their frequency.

While the radiative effect of clouds is dependent on many factors [e.g. *Shupe and Intrieri*, 2004], clouds over the GrIS have been found to increase meltwater runoff by one third relative to clear skies after accounting for their effect on refreezing [*Van Tricht et al.*, 2016]. This suggests

that the observed meltwater increase between our two ten-year periods has occurred largely despite a weak decrease in cloud fraction rather than in response to it. The greatest increase in LW radiation occurred over northwestern Greenland where cloud fraction also increased, but LW radiation increased elsewhere despite decreased cloud fraction. Therefore, it is likely that increased LW radiation is at least partially due to increased large-scale energy transport into the region. In addition, this energy balance term is indistinguishable from greenhouse gas forcing, which likely is playing a role in the surface warming.

The large increases in net radiation in the ablation zone are likely mostly due to decreasing albedo, with the remainder of the ice sheet able to reflect most of the increased insolation. Conversely, the tundra absorbs most of the increased insolation, though it is able to partially offset increased downwelling LW radiation with increased LW emission. The albedo of much of the ablation zone has been found to be decreasing at a statistically significant rate in approximately the same time period, primarily related to endogenous processes [*Tedesco et al.*, 2016]. This feedback between increased melt and albedo is amplified in periods of persistent atmospheric ridging as occurred for extended periods in the summers of 2007-2012 because reduced snowfall sustains the low albedo, and increased warm air advection increases sensible heating which enhances snow grain metamorphic rates [*Box et al.*, 2012; *van Angelen et al.*, 2014]. While albedo is not analyzed explicitly here, net radiation provides the best insight into the importance of albedo within the context of this study, and increases in net radiation in the highest thermodynamic nodes are substantial.

6. Conclusions

We have applied self organizing map analysis to attribute trends in summer GrIS surface melt from a synoptic climatology perspective. Using melt anomaly composites applied to the SOM nodes obtained from 500 hPa anomalies, we find a strong preference for anomalous surface melt with a mid-level ridge oriented over Greenland up to the pole and west to the Beaufort Sea, which is in line with previous studies. Some of these nodes exhibit statistically significant trends, particularly an increasing (decreasing) frequency of a ridge (trough) over Greenland. We show that these atmospheric patterns are associated with suppressed cloud cover and increased insolation associated with higher temperatures and humidity. Furthermore, atmospheric patterns favoring melt occur simultaneously with wind, temperature and humidity distributions suggestive of large-scale advection of heat and moisture at mid-levels in the atmosphere, particularly over the western ice sheet.

Between 1979-1988 and 2005-2014, summer surface mass loss from MAR simulations has increased from an ice sheet average of 164 Gt to 267 Gt (62.8% increase). We attribute 77.5 Gt (75.0%) of this increase to thermodynamics, 17.4 Gt (16.9%) to dynamics, and 8.3 Gt (8.0%) to a combination of these terms. There is also an 18% increase in grid cells exceeding the 1 mm day^{-1} threshold as melt has more frequently extended farther up the ice sheet. A detailed analysis of these two time periods suggests that this increase from dynamics is primarily from a large and statistically significant increase in frequency over three SOM nodes that feature 500 hPa ridging from Greenland to the pole and west to the Beaufort Sea.

The total increase in surface melt has accelerated since 2007 as the synoptic pattern has been more conducive to GrIS melt, but the dynamics term is still small relative to the thermodynamic term when summed over all 30 SOM nodes, which accounts for the majority of the total

melt. The primary drivers of the increased melt from thermodynamics were found to be increased insolation, longwave radiation (despite decreased cloud fraction), and net radiation likely resulting most from a darkening of the ice sheet, all resulting in a 3-5 °C increase in near-surface temperature. Given that the thermodynamics term still accounted for the majority of the increased surface melt during this period, we expect an overall continued acceleration in GrIS surface mass loss regardless of future changes in the Arctic atmospheric circulation.

Acknowledgments

References

Abdalati, W., and K. Steffen (2001), Greenland ice sheet melt extent: 1979-1999, *J. Geophys. Res.*, 106(D24), 33983–33988.

van Angelen, J. H., M. R. van den Broeke, and W. J. van de Berg (2011), Momentum budget of the atmospheric boundary layer over the Greenland ice sheet and its surrounding seas, *J. Geophys. Res.*, 116, D10101, doi:10.1029/2010JD015485.

van Angelen, J. H., J. T. M. Lenaerts, M. R. van den Broeke, and B. Wouters (2013), Contemporary (1960–2012) evolution of the climate and surface mass balance of the Greenland ice sheet, *Surv. Geophys.*, doi:10.1007/s10712-013-9261-z.

Belleflamme, A., Fettweis, X., and M. Erpicum (2015), Recent summer Arctic atmospheric circulation anomalies in a historical perspective, *Cryosph.*, 53-64, doi:10.5194/tc-9-53-2015.

Bhattacharya, I., K. C. Jezek, L. Wang, and H. Liu (2009), Surface melt area variability of the Greenland ice sheet: 1979-2009, *Geophys. Res. Lett.*, 36(L20502).

Bosilovich, M. G., F. R. Robertson, and J. Chen (2011), Global Energy and Water Budgets in MERRA, *J. Clim.*, 24(22), 5721–5739, doi:10.1175/2011JCLI4175.1.

Box, J. E., et al. (2006), Greenland ice sheet surface mass balance variability (1988–2004) from calibrated polar MM5 output, *J. Clim.*, 19, 2783–2800.

Box, J. E., X. Fettweis, J. C. Stroeve, M. Tedesco, D. K. Hall, and K. Steffen (2012), Greenland ice sheet albedo feedback: Thermodynamics and atmospheric drivers, *Cryosph.*, 6, 593–634, doi:10.5194/tcd-6-593-2012.

van den Broeke, M. R., and H. Gallée (1996), Observation and simulation of barrier winds at the western margin of the Greenland ice sheet, *Q. J. R. Meteorol. Soc.*, 122, 1365–1383.

van den Broeke, M., J. Bamber, J. Ettema, E. Rignot, E. Schrama, W. J. van de Berg, E. van Meijgaard, I. Velicogna, and B. Wouters (2009), Partitioning recent Greenland mass loss, *Science*, 326(5955), 984–986, doi:10.1126/science.1178176.

van den Broeke, M. R., C. J. P. P. Smeets, and R. S. W. van de Wal (2011), The seasonal cycle and interannual variability of surface energy balance and melt in the ablation zone of the west Greenland ice sheet, *Cryosph.*, 5(2), 377–390, doi:10.5194/tc-5-377-2011.

van den Broeke, M., P. Duynkerke, and J. Oerlemans (1994), The observed katabatic flow at the edge of the Greenland ice sheet during GIMEX-91, *Glob. Planet. Change*, 9(1-2), 3–15, doi:10.1016/0921-8181(94)90003-5.

van den Broeke, M., P. Smeets, and J. Ettema (2009), Surface layer climate and turbulent exchange in the ablation zone of the west Greenland ice sheet, *Int. J. Climatol.*, 29(15), 2309–2323, doi:10.1002/joc.1815.

Brun, E., David, P., Sudul, M., and G. Brunot (1992), A numerical model to simulate snow-cover stratigraphy for operational avalanche forecasting. *J. Glaciol.*, *38*(128), 13–22.

Cassano, J. J., P. Uotila, and A. Lynch (2006), Changes in synoptic weather patterns in the polar regions in the twentieth and twenty-first centuries, part 1: Arctic, *Int. J. Clim.*, 1049(March), 1027–1049, doi:10.1002/joc.1306.

Cassano, J. J., P. Uotila, A. H. Lynch, and E. N. Cassano (2007), Predicted changes in synoptic forcing of net precipitation in large Arctic river basins during the 21st century, *J. Geophys. Res. Biogeosciences*, 112(4), 1–20, doi:10.1029/2006JG000332.

Cullather, R. I., and M. G. Bosilovich (2011), The Moisture Budget of the Polar Atmosphere in MERRA, *J. Clim.*, 24(11), 2861–2879, doi:10.1175/2010JCLI4090.1.

Cullather, R. I., and M. G. Bosilovich (2012), The Energy Budget of the Polar Atmosphere in MERRA, *J. Clim.*, 25(1), 5–24, doi:10.1175/2011JCLI4138.1.

Day, J. J., J. L. Bamber, and P. J. Valdes (2013), The Greenland Ice Sheet's surface mass balance in a seasonally sea ice-free Arctic, *J. Geophys. Res. Earth Surf.*, 118(3), 1533–1544, doi:10.1002/jgrf.20112.

de Ridder, K., and H. Gallée (1998), Land surface-induced regional climate change in southern Israel. *J. Appl. Meteorol.*, *37*(11), 1470-1485.

Deser, C., J. E. Walsh, and M. S. Timlin (2000), Arctic Sea Ice Variability in the Context of Recent Atmospheric Circulation Trends, *J. Clim.*, 13, 617–633.

Ettema, J., M. R. van den Broeke, E. van Meijgaard, W. J. van de Berg, J. L. Bamber, J. E. Box, and R. C. Bales (2009), Higher surface mass balance of the Greenland ice sheet revealed by high-resolution climate modeling, *Geophys. Res. Lett.*, 36(12), L12501, doi:10.1029/2009GL038110.

Ettema, J., M. R. van den Broeke, E. van Meijgaard, and W. J. van de Berg (2010), Climate of the Greenland ice sheet using a high-resolution climate model–Part 2: Near-surface climate and energy balance, *Cryosph*, 4(4), 529–544, doi:10.5194/tc-4-529-2010.

Fang Z-F (2004). Statistical relationship between the northern hemisphere sea ice and atmospheric circulation during wintertime. In: Observation, Theory and Modeling of Atmospheric Variability. World Scientific Series on Meteorology of East Asia, Zhu X (ed), World Scientific.

Fettweis, X., H. Gallée, L. Lefebre, and J. P. van Ypersele (2005), Greenland surface mass balance simulated by a regional climate model and comparison with satellite derived data, *Clim. Dyn.*, 24, 623–640, doi:10.1007/s00382-005-0010-y.

Fettweis, X., M. Tedesco, M. van den Broeke, and J. Ettema (2011a), Melting trends over the Greenland ice sheet (1958–2009) from spaceborne microwave data and regional climate models, *Cryosph.*, 5(2), 359–375, doi:10.5194/tc-5-359-2011.

Fettweis, X., G. Mabille, M. Erpicum, S. Nicolay, and M. van den Broeke (2011b), The 1958-2009 Greenland ice sheet surface melt and the mid-tropospheric atmospheric circulation, Clim. Dyn., 36(1), 139–159, doi:10.1007/s00382-010-0772-8.

Fettweis, X., E. Hanna, C. Lang, A. Belleflamme, M. Erpicum, and H. Gallée (2013), Brief communication Important role of the mid-tropospheric atmospheric circulation in the recent surface melt increase over the Greenland ice sheet, *Cryosphere*, 7(1), 241–248, doi:10.5194/tc-7-241-2013.

Francis, J. A., and S. J. Vavrus (2012), Evidence linking Arctic amplification to extreme weather in mid-latitudes, *Geophys. Res. Lett.*, 39(L06801), 1–6, doi:10.1029/2012GL051000.

Francis, J. A., and S. J. Vavrus (2015), Evidence for a wavier jet stream in response to rapid Arctic warming, *Env. Res. Lett.*, doi:10.1088/1748-9326/10/1/014005

Franco, B., X. Fettweis, and M. Erpicum (2013), Future projections of the Greenland ice sheet energy balance driving the surface melt, *Cryosphere*, 7(1), 1–18, doi:10.5194/tc-7-1-2013.

Gallée, H., and G. Schayes (1994), Development of a three-dimensional meso-γ primitive equation model – katabatic winds simulation in the area of Terra-Nova Bay, Antarctica. *Mon. Wea. Rev.*, *122*(4), 671-685.

Gallée H., Peyaud V., and I. Goodwin (2005), Simulation of the net snow accumulation along the Wilkes Land transect, Antarctica, with a regional climate model. *Ann. Glaciol.*, *41*,17-22.

Gorter, W., J. H. van Angelen, J. T. M. Lenaerts, and M. R. van den Broeke (2014), Present and future near-surface wind climate of Greenland from high resolution regional climate modelling, *Clim. Dyn.*, 42(5-6), 1595–1611, doi:10.1007/s00382-013-1861-2.

Hall, R., Erdélyi, R., Hanna, E., Jones, J. M., and A. A.Scaife (2015), Drivers of North Atlantic Polar Front jet stream variability. *Int. J. Climatol.*, 35: 1697-1720. doi: 10.1002/joc.4121.

Hanna, E., P. Huybrechts, K. Steffen, J. Cappelen, R. Huff, C. Shuman, T. Irvine-Fynn, S. Wise, and M. Griffiths (2008), Increased Runoff from Melt from the Greenland Ice Sheet: A Response to Global Warming, *J. Clim.*, 21(2), 331–341, doi:10.1175/2007JCLI1964.1.

Hanna, E., J. M. Jones, J. Cappelen, S. H. Mernild, L. Wood, K. Steffen, and P. Huybrechts (2013), The influence of North Atlantic atmospheric and oceanic forcing effects on 1900-2010 Greenland summer climate and ice melt/runoff, *Int. J. Climatol.*, 33(4), 862–880, doi:10.1002/joc.3475.

Hanna, E., F.J. Navarro, F. Pattyn, C. Domingues, X. Fettweis, E. Ivins, R.J. Nicholls, C. Ritz, B. Smith, S. Tulaczyk, P. Whitehouse and J. Zwally (2013b), Ice-sheet mass balance and climate change, *Nature*, 498, 51-59.

Hanna, E., X. Fettweis, S. H. Mernild, J. Cappelen, M. H. Ribergaard, C. a. Shuman, K. Steffen, L. Wood, and T. L. Mote (2014), Atmospheric and oceanic climate forcing of the exceptional Greenland ice sheet surface melt in summer 2012, *Int. J. Climatol.*, 34(4), 1022–1037, doi:10.1002/joc.3743.

Hanna, E., Cropper, T. E., Jones, P. D., Scaife, A. A., and R. Allan (2015), Recent seasonal asymmetric changes in the NAO (a marked summer decline and increased winter variability) and associated changes in the AO and Greenland Blocking Index. *Int. J. Climatol.*, 35, 2540-2554. doi: 10.1002/joc.4157.

Higgins, M. E., and J. J. Cassano (2009), Impacts of reduced sea ice on winter Arctic atmospheric circulation, precipitation, and temperature, *J. Geophys. Res.*, 114(D16), D16107, doi:10.1029/2009JD011884.

Horton, D. E., N. C. Johnson, D. Singh, D. L. Swain, B. Rajaratnam, and N. S. Diffenbaugh (2015), Contribution of changes in atmospheric circulation patterns to extreme temperature trends, *Nature*, 522(7557), 465–469, doi:10.1038/nature14550.

Jeffries, M.O., and J. Richter-Menge, Eds., 2015: The Arctic [in "State of the Climate in 2014"]. *Bull. Amer. Meteor. Soc.*, 96(7), S169-S219.

Johnson, N. C., S. B. Feldstein, and B. Tremblay (2008), The continuum of northern hemisphere teleconnection patterns and a description of the NAO shift with the use of self-organizing maps, J. Clim., 21(23), 6354–6371, doi:10.1175/2008JCLI2380.1.

Kennedy, A. D., X. Dong, B. Xi, S. Xie, Y. Zhang, and J. Chen (2011), A Comparison of MERRA and NARR Reanalyses with the DOE ARM SGP Data, *J. Clim.*, 24(17), 4541–4557, doi:10.1175/2011JCLI3978.1.

Koenig, S. J., R. M. Deconto, and D. Pollard (2014), Impact of reduced Arctic sea ice on Greenland ice sheet, *Geophys. Res. Lett.*, 41(10.1002/2014GL059770), 3934–3943, doi:10.1002/2014GL059770.A.

Kohonen, T. (2001), Self-Organizing Maps, Self-organizing maps. 3rd ed. Berlin: Springer, 2001, 501 p. Springer series in information sciences, ISBN 3540679219, 1.

Lefebre, F., Gallée, H., van Ypersele, J.P., and W. Greuell (2003), Modeling of snow and ice melt at ETH-Camp (West Greenland): A study of surface albedo. *J. Geophys. Res.*,

108(D8), 4231.doi:10.1029/2001JD001160.

Lefebre, F., Fettweis, X., Galée, H., van Ypersele, J.-P., Marbaix, P., Greuell, W., and P. Calanca, (2005), Evaluation of a high-resolution regional climate simulation over Greenland. *Clim. Dyn., 25*(1), 99-116. doi:10.1007/s00382-005-0005-8.

Lindsay, R., M. Wensnahan, A. Schweiger, and J. Zhang (2014), Evaluation of Seven Different Atmospheric Reanalysis Products in the Arctic*, *J. Clim.*, 27(7), 2588–2606, doi:10.1175/JCLI-D-13-00014.1.

McLeod, J. T., and T. L. Mote (2015), Linking interannual variability in extreme Greenland blocking episodes to the recent increase in summer melting across the Greenland ice sheet, *Int. J. Climatol.*, doi:10.1002/joc.4440.

Mernild, S. H., T. L. Mote, and G. E. Liston (2011), Greenland ice sheet surface melt extent and trends: 1960–2010, J. Glaciol., 57(204), 621–628, doi:10.3189/002214311797409712.

Mills, C. M., and J. E. Walsh (2014), Synoptic Activity Associated with Sea Ice Variability in the Arctic, J. Geophys. Res. Atmos., 119(21), 12,117–12,131, doi:10.1002/2014JD021604.

Mote, T. L. (1998a), Mid - tropospheric circulation and surface melt on the Greenland ice sheet. Part I: atmospheric teleconnections, *Int. J. Clim.*, 18, 111–129, doi:10.1002/(SICI)1097-0088(199802)18.

Mote, T. L. (1998b), Mid-tropospheric circulation and surface melt on the Greenland ice sheet. Part II: synoptic climatology, *Int. J. Climatol.*, 18(2), 131–145, doi:10.1002/(SICI)1097-0088(199802)18.

Mote, T. L. (2007), Greenland surface melt trends 1973-2007: Evidence of a large increase in 2007, *Geophys. Res. Lett.*, 34(L22507), 10.1029/2007GL031976.

Neff, W., G. P. Compo, R. M. Ralph, and M. D. Shupe (2014), Continental heat anomalies and the extreme melting of the Greenland ice surface in 2012 and 1889, *J. Geophys. Res. Atmos.*, 119, 6520–6536, doi:10.1002/2014JD021470.

Noël, B., X. Fettweis, W. J. van de Berg, M. R. van den Broeke, and M. Erpicum (2014), Small impact of surrounding oceanic conditions on 2007–2012 Greenland Ice Sheet surface mass balance, *Cryosph.*, 8(2), 1453–1477, doi:10.5194/tcd-8-1453-2014.

Orr, A., Hanna, E., Hunt, J.C.R., Cappelen, J., Steffen, K. and A.G. Stephens (2005), Characteristics of stable flows over southern Greenland. *Pure Appl. Geophys.*, 162(10), 1747-1778, doi:10.1007/s00024-005-2691-x.

Overland, J. E., J. a. Francis, E. Hanna, and M. Wang (2012), The recent shift in early summer Arctic atmospheric circulation, *Geophys. Res. Lett.*, 39(19), 1–6, doi:10.1029/2012GL053268.

Overland, J., E. Hanna, I. Hanssen-Bauer, S.-J. Kim, J.E. Walsh, M. Wang, U.S. Bhatt, and R.L. Thoman (2015a), Surface Air Temperature [in Arctic Report Card 2015], http://www.arctic.noaa.gov/reportcard/air_temperature.html.

Overland, J., J.A. Francis, R. Hall, E. Hanna, J.-J. Kim, and T. Vihma (2015), The melting Arctic and midlatitude weather patterns: are they connected? *J. Clim.*, 28, 7917-7932.

Pithan, F., and T. Mauritsen (2014), Arctic amplification dominated by temperature feedbacks in

contemporary climate models, *Nature Geosci.*, 7, 181–184, doi:10.1038/NGEO2071.

Rajewicz, J., and S. J. Marshall (2014), Variability and trends in anticyclonic circulation over the Greenland ice sheet, 1948-2013, Geophys. Res. Lett., 41, 2842–2850, doi:10.1002/2013GL058954.

Reichle, R. H., R. D. Koster, G. J. M. De Lannoy, B. a. Forman, Q. Liu, S. P. P. Mahanama, and A. Touré (2011), Assessment and Enhancement of MERRA Land Surface Hydrology Estimates, J. Clim., 24(24), 6322–6338, doi:10.1175/JCLI-D-10-05033.1.

Rennermalm, A. K., L. C. Smith, J. C. Stroeve, and V. W. Chu (2009), Does sea ice influence Greenland ice sheet surface-melt?, *Environ. Res. Lett.*, 4(2), 024011, doi:10.1088/1748-9326/4/2/024011.

Rienecker, M. M. et al. (2011), MERRA - NASA's Modern-Era Retrospective Analysis for Research and Applications, *J. Clim.*, 24, 3624–3648, doi:10.1175/JCLI-D-11-00015.1.

Rignot, E., I. Velicogna, M. R. van den Broeke, A. Monaghan, and J. Lenaerts (2011), Acceleration of the contribution of the Greenland and Antarctic ice sheets to sea level rise, *Geophys. Res. Lett.*, 38(5), 1–5, doi:10.1029/2011GL046583.

Rinke, A., W. Maslowski, K. Dethloff, and J. Clement (2006), Influence of sea ice on the atmosphere: A study with an Arctic atmospheric regional climate model, *J. Geophys. Res.*, 111(D16), D16103, doi:10.1029/2005JD006957.

Schuenemann, K. C., and J. Cassano (2009), Changes in synoptic weather patterns and Greenland precipitation in the 20th and 21st centuries: 1. Evaluation of late 20th century simulations from IPCC models, *J. Geophys. Res.*, 114(D20113), 10.1029/2009JD011705.

Schuenemann, K. C., J. J. Cassano, and J. Finnis (2009), Synoptic Forcing of Precipitation over Greenland: Climatology for 1961–99, *J. Hydrometeorol.*, 10(1), 60–78, doi:10.1175/2008JHM1014.1.

Serreze, M. C., and J. A. Francis (2006), The Arctic Amplification Debate, *Clim. Change*, 76(3-4), 241–264, doi:10.1007/s10584-005-9017-y.

Serreze, M. C., A. P. Barrett, J. C. Stroeve, D. N. Kindig, and M. M. Holland (2009), The emergence of surface-based Arctic amplification, *Cryosph.*, 3, 11–19.

Shupe, M. D., and J. M. Intrieri (2004), Cloud radiative forcing of the Arctic surface: The influence of clouds properties, surface albedo, and solar zenith angle, *J. Clim.*, 17, 616–628, doi:10.1175/1520-0442(2004)017<0616:CRFOTA>2.0.CO;2.

Skific, N., J. A. Francis, and J. J. Cassano (2009), Attribution of Projected Changes in Atmospheric Moisture Transport in the Arctic: A Self-Organizing Map Perspective, *J. Clim.*, 22(15), 4135–4153, doi:10.1175/2009JCLI2645.1.

Tedesco, M., M. Serreze, and X. Fettweis (2008), Diagnosing the extreme surface melt event over southwestern Greenland in 2007, *Cryosph.*, 2(2), 159–166.

Tedesco, M., X. Fettweis, M. R. van den Broeke, R. S. W. van de Wal, C. J. P. P. Smeets, W. J. van de Berg, M. C. Serreze, and J. E. Box (2011), The role of albedo and accumulation in the 2010 melting record in Greenland, *Environ. Res. Lett.*, 6(1), 014005, doi:10.1088/1748-9326/6/1/014005.

Tedesco, M., X. Fettweis, T. Mote, J. Wahr, P. Alexander, J. E. Box, and B. Wouters (2013), Evidence and analysis of 2012 Greenland records from spaceborne observations, a regional climate model and reanalysis data, Cryosph., 7(2), 615–630, doi:10.5194/tc-7-615-2013.

Tedesco, M. et al. (2014), Greenland, in State of the Climate 2013. *Bull. Amer. Meteor. Soc.,* 95.

Tedesco, M., S. Doherty, X. Fettweis, P. Alexander, J. Jeyaratnam, and J. Stroeve (2016), The darkening of the Greenland ice sheet: trends, drivers, and projections (1981-2100), *Cryosph.*, 10, 477-496, doi:10.5194/tc-10-477-2016.

Van Tricht, K., S. Lhermitte, J.T.M. Lenaerts, I.V. Gorodetskaya, T.S. T'Ecuyer, B. Noël, M.R. van den Broeke, D.D. Turner, and N.P.M. van Lipzig (2016), Clouds enhance Greenland ice sheet meltwater runoff, Nat. Commun., 7, 10266, doi:10.1038/ncomms10266.

Zib, B. J., X. Dong, B. Xi, and A. Kennedy (2012), Evaluation and Intercomparison of Cloud Fraction and Radiative Fluxes in Recent Reanalyses over the Arctic Using BSRN Surface Observations, *J. Clim.*, 25(7), 2291–2305, doi:10.1175/JCLI-D-

Figures
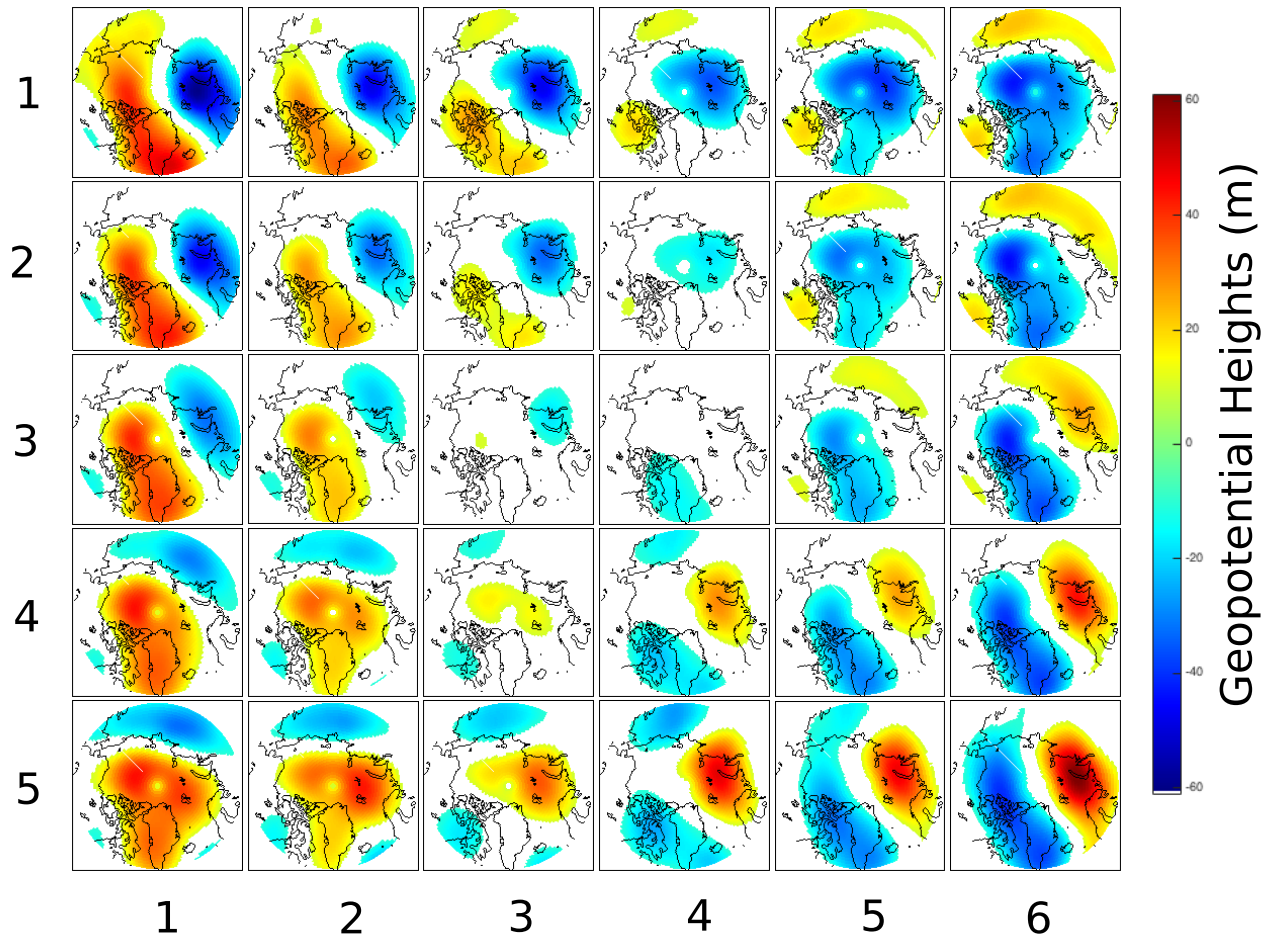
Fig. 1: Master map of SOM nodes obtained from daily JJA 500 hPa geopotential height anomalies (1979-2014).
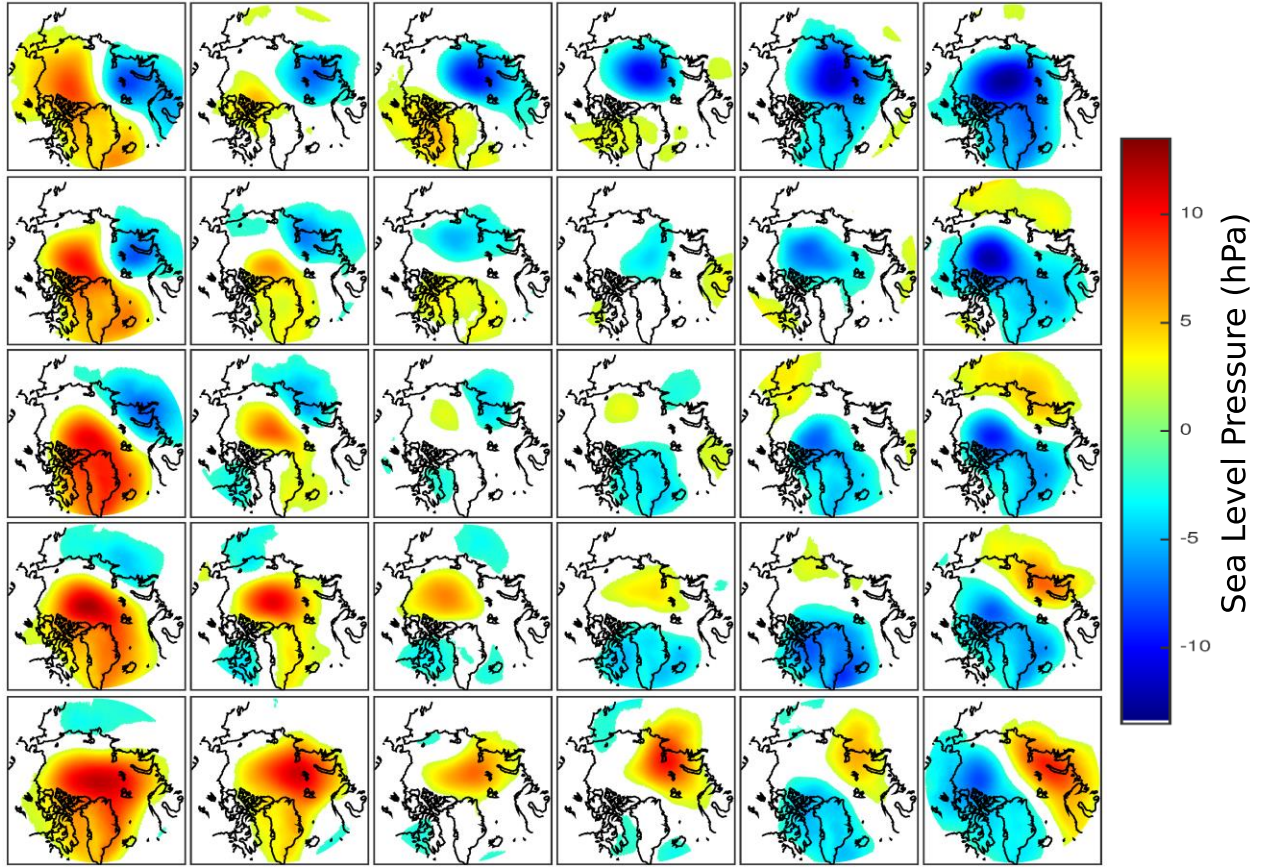
Fig. 2: MERRA sea level pressure anomalies mapped to their best matching node and averaged over all dates.
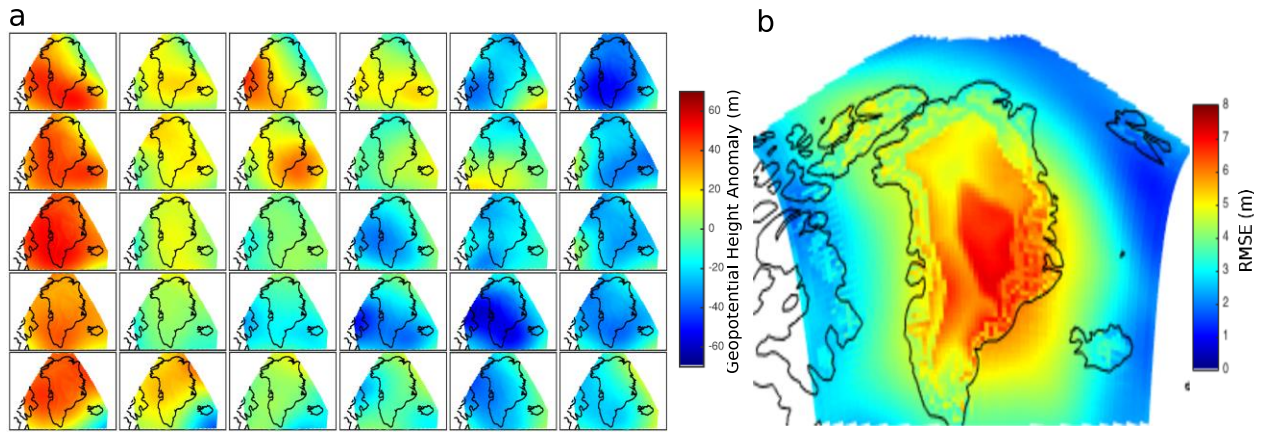
Fig. 3: (a) MAR 500 hPa height anomalies mapped to their best matching node and averaged over all dates. (b) Root Mean Square Error of node-averaged MAR 500 hPa geopotential height anomalies from those of MERRA after regridding.
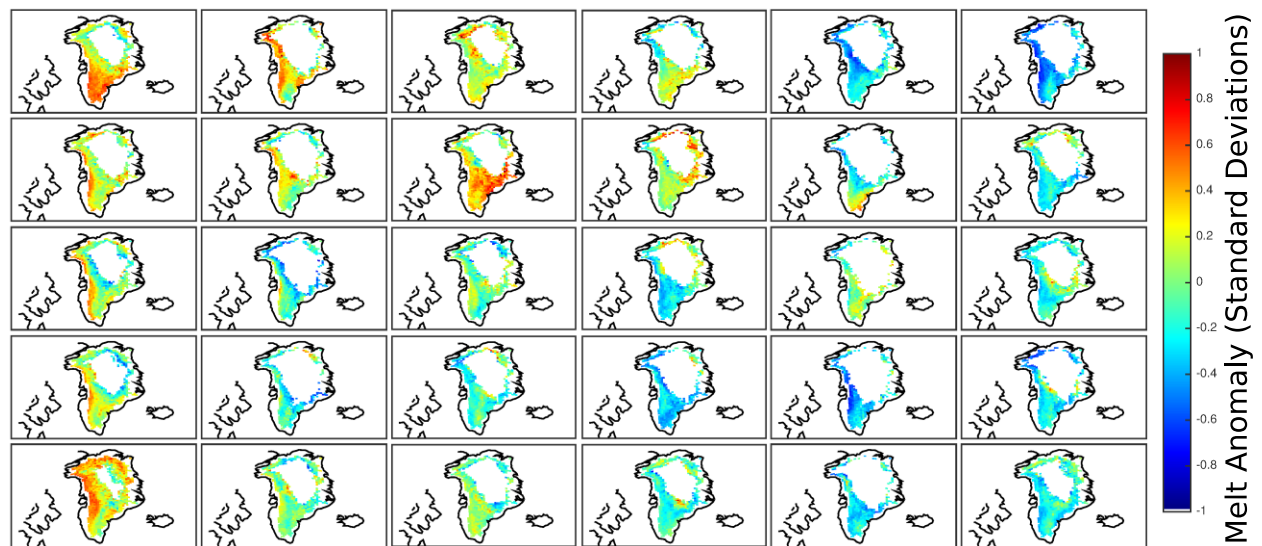

Fig. 4: Daily standardized meltwater production anomalies mapped to their best matching node and averaged over all dates. Grid cells with fewer than 10 non-zero meltwater production values are masked.
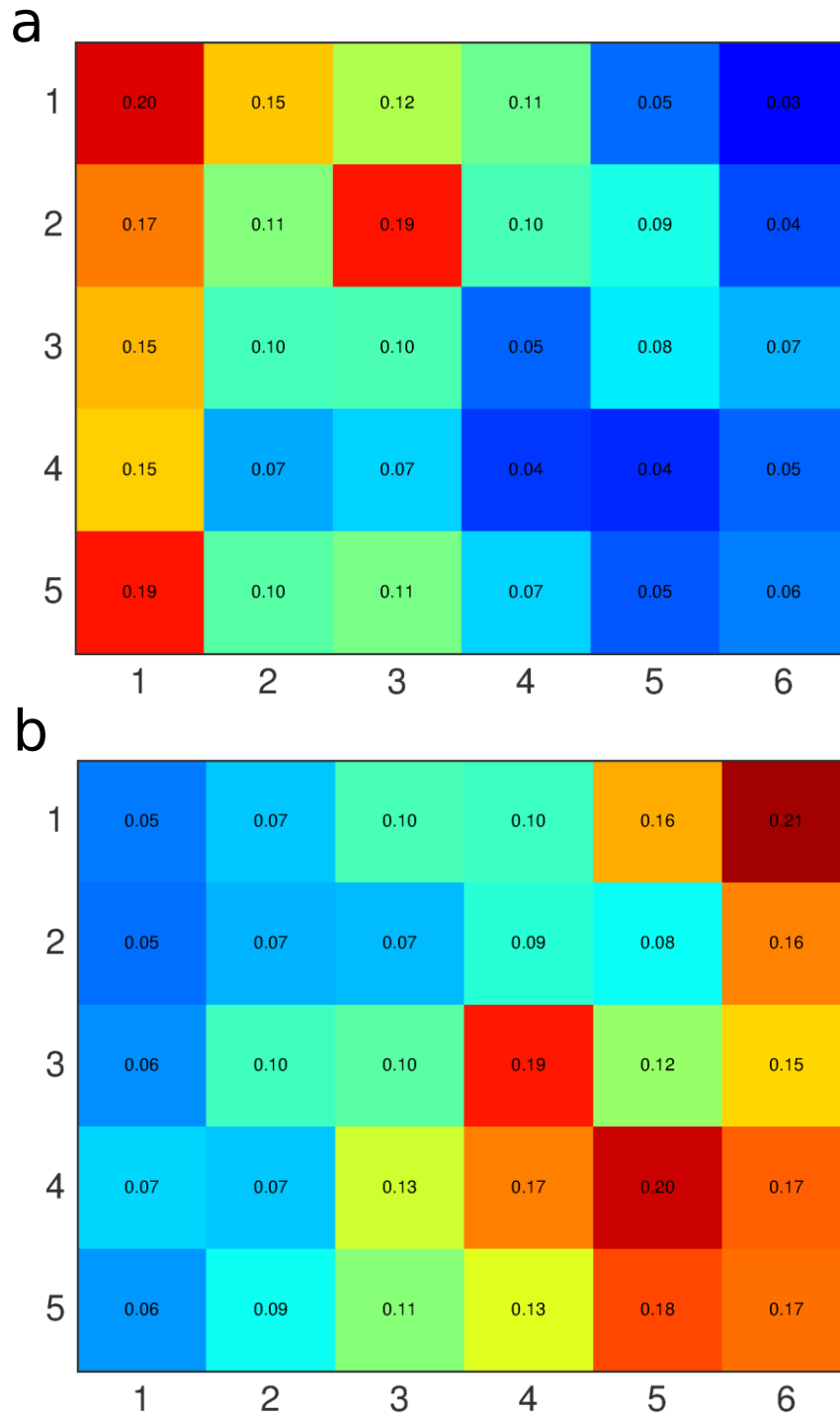
Fig. 5: Fraction of occurrence of area-averaged meltwater production anomalies greater (a) and less (b) than 1 standard deviation of the mean for each SOM node.
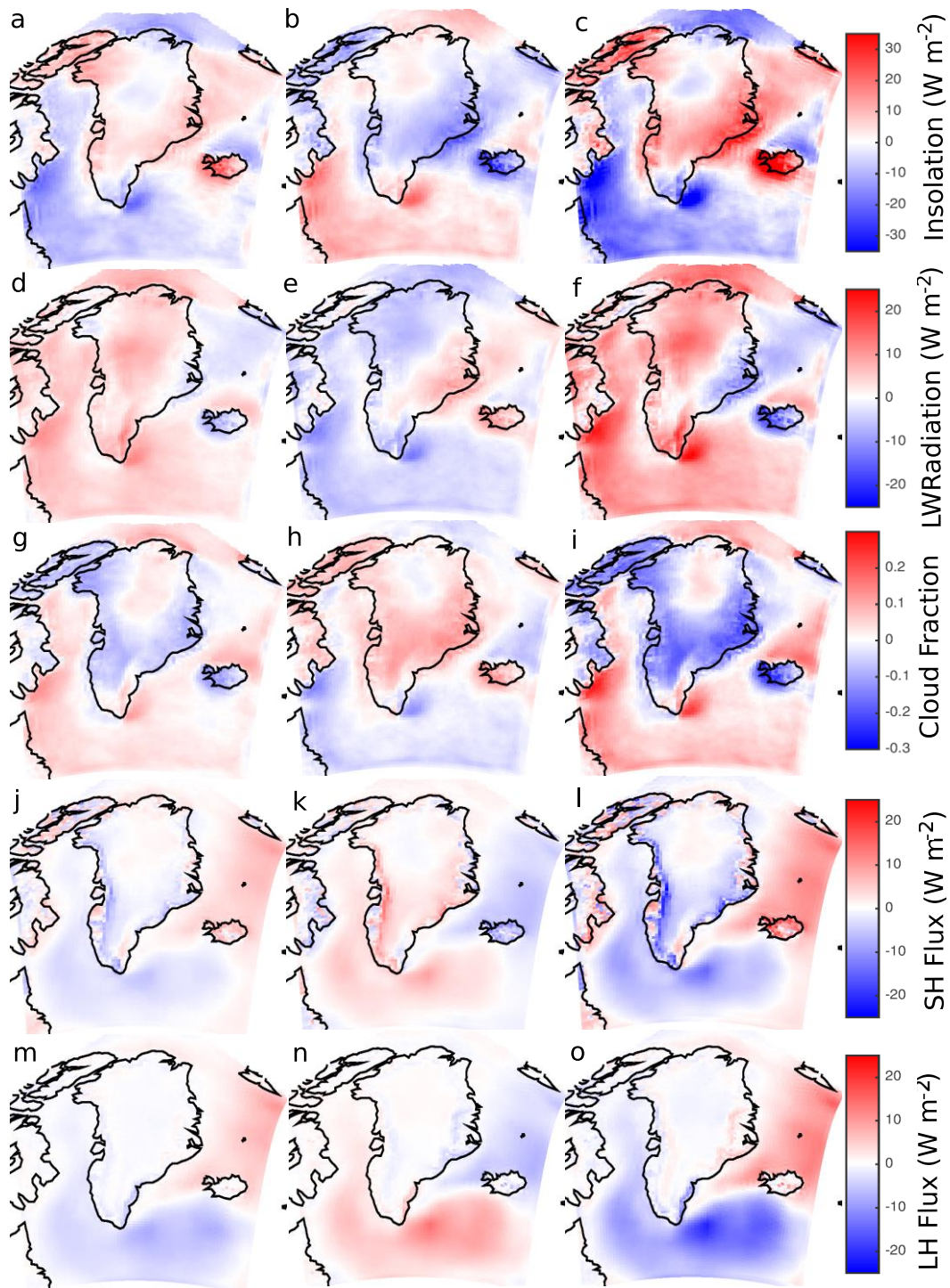
Fig. 6: Composite anomalies of insolation in high melt nodes (a), low melt nodes (b), and their difference (c), downwelling longwave radiation (d,e,f), cloud fraction (g,h,i), sensible heat flux (j,k,l), and latent heat flux (m,n,o). Positive latent and sensible fluxes are directed upwards.
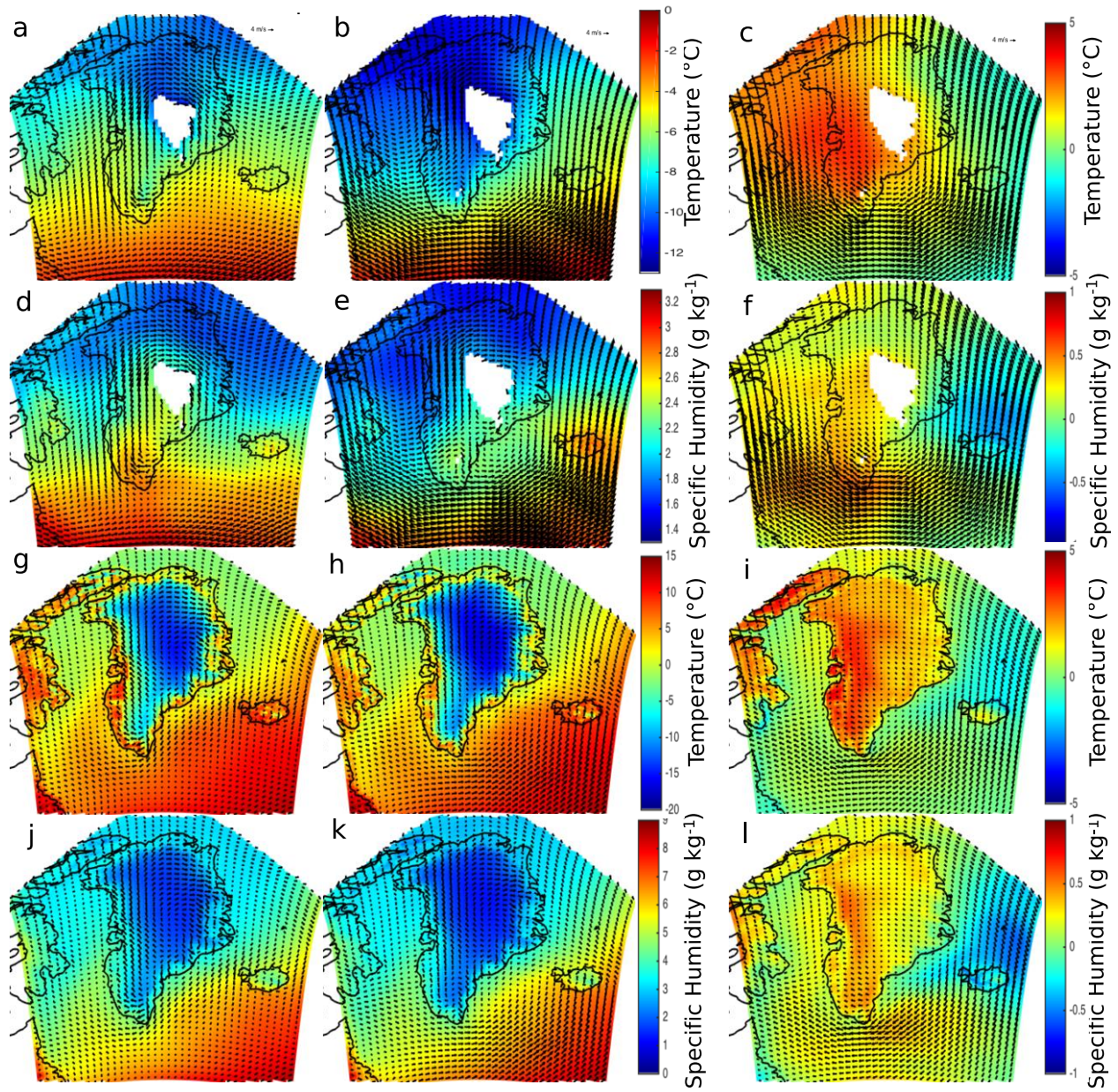
Fig. 7: Composite 700 hPa (top) and 10 m (bottom) wind vectors in high melt nodes (first column) low melt nodes (second column), and their difference (third column) overlaid on the composite 700 hPa (top) and 10 m (bottom) temperature and specific humidity fields. White areas are above the mean 700 hPa level.
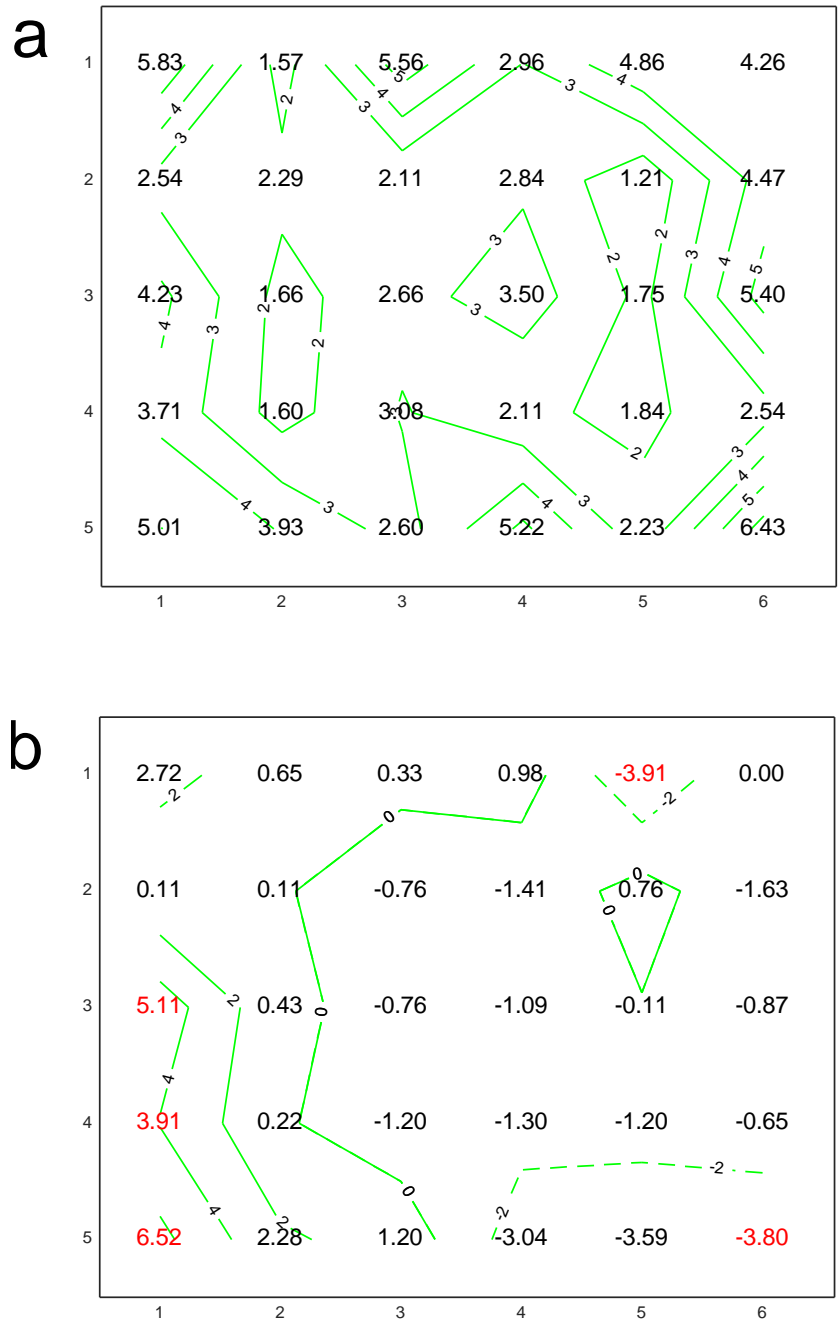
Fig. 8: JJA 500 hPa geopotential height anomaly SOM pattern frequencies for a) the 1979-2014 period, b) difference in pattern frequencies between dates between the 1979-1988 and 2005-2014 periods. Differences significant at alpha = 0.05 are highlighted. The position of each number corresponds with the synoptic pattern of the same position in the master SOM in Fig. 1.
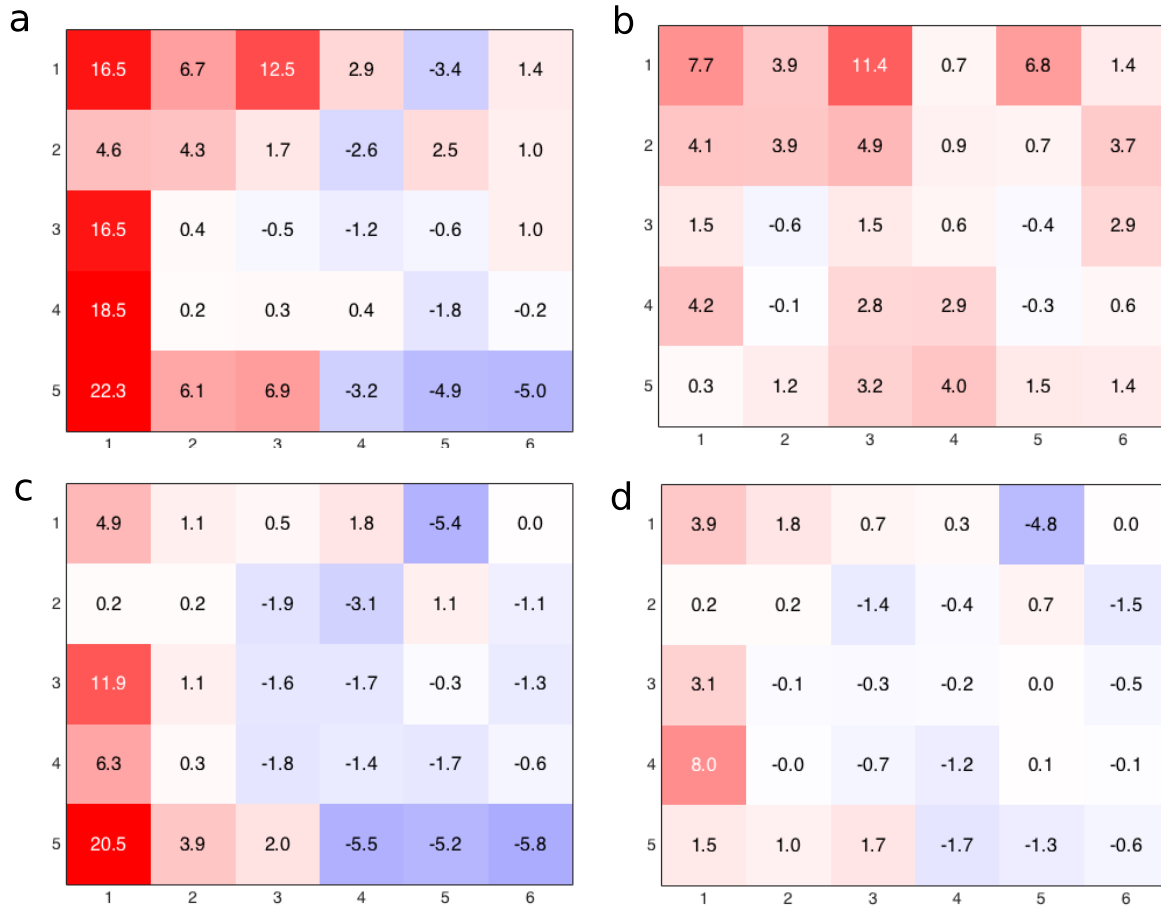
Fig. 9: The change in each 500 hPa geopotential height anomaly SOM node of JJA net meltwater production (Gt) parsed into its components of (a) total change, (b) thermodynamic change, (c) dynamic change, and (d) dynamic change acting on thermodynamic change averaged over Greenland between 1979-1988 versus 2005-2014.
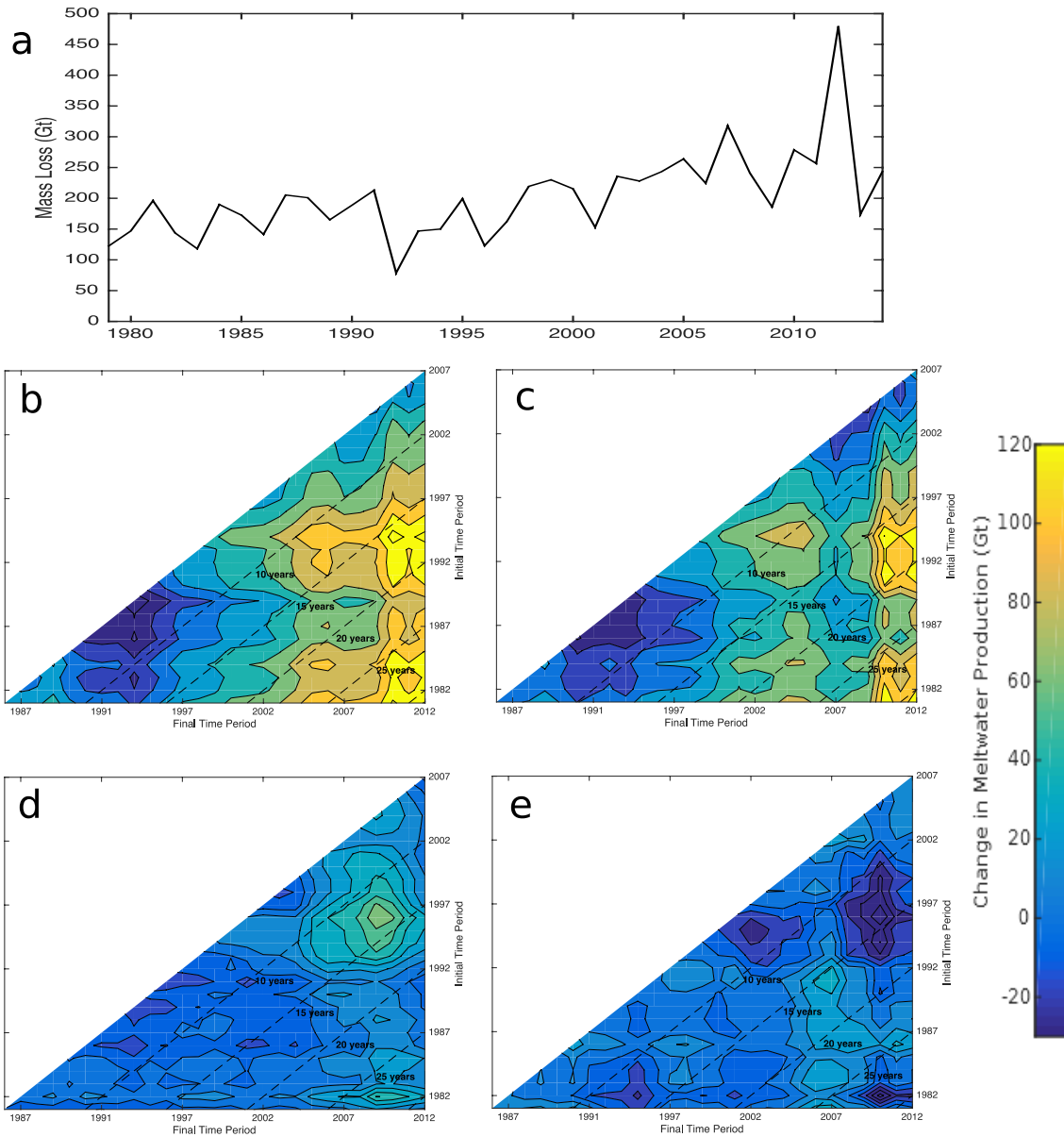
Fig. 10: (a) time series of ice sheet mean JJA mass loss, and (b) total change, (c) thermodynamic change, (d) dynamic change, and (e) dynamic change acting on thermodynamic change of JJA meltwater production (Gt) summed over the GrIS and summed across all SOM nodes as a function of the initial and final periods chosen for comparison. Each time period is 5 years in length, with the middle year in the period corresponding to dates on the axes. Dashed lines display the length of time between the two periods.
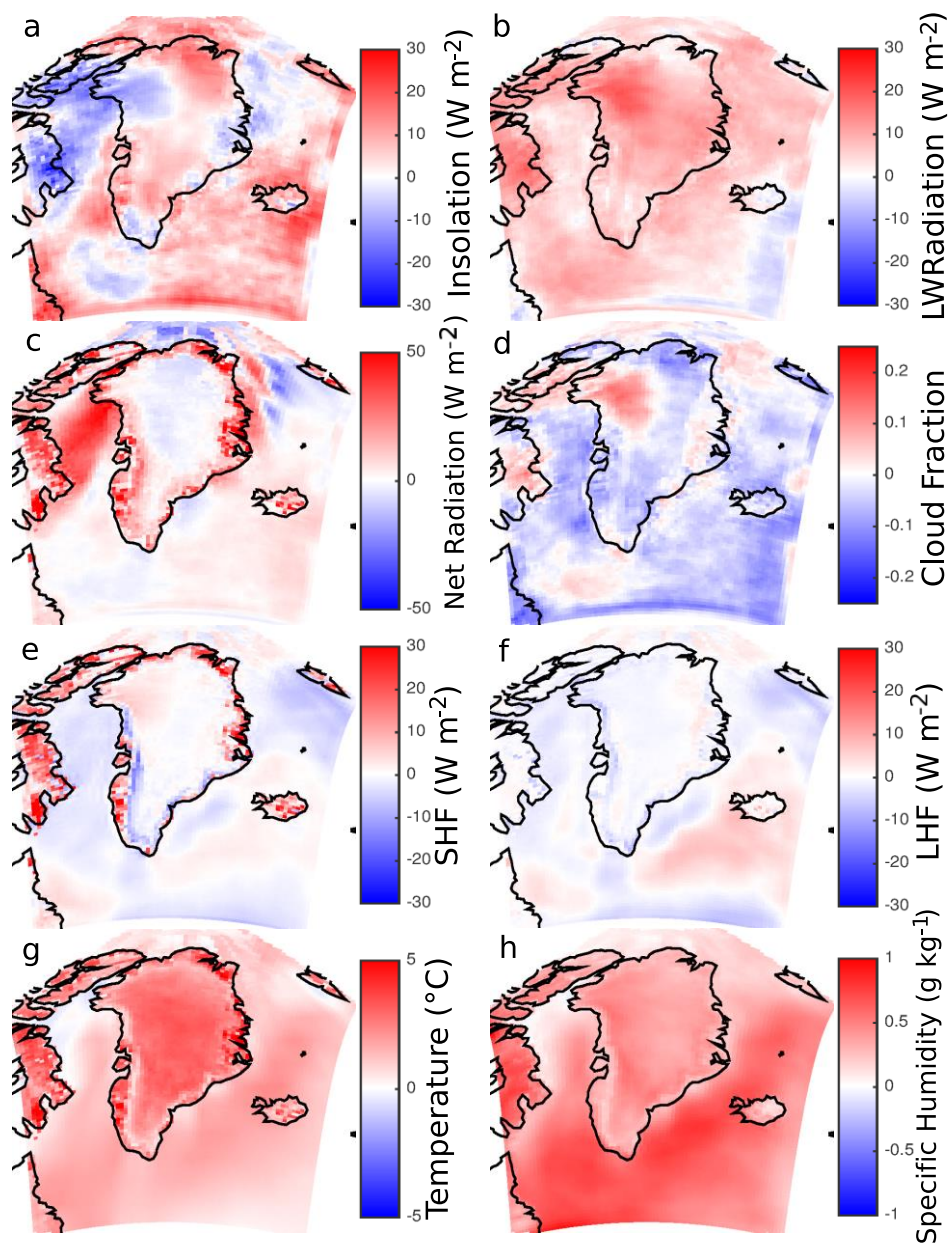
Fig 11: Node-composited change in insolation (a), downwelling longwave radiation (b), net radiation (c), cloud fraction (d), sensible heat flux (e), latent heat flux (f), 10 m temperature (g), and 10 m specific humidity (h) between 1979-1988 and 2005-2014. Positive latent and sensible fluxes are directed upwards. Composites are drawn from the three nodes ((1,1), (1,3), (1,5)) of Fig. 9b with the greatest increase in the thermodynamic component.